Resource

SOURCE DATA | TRANSPARENT PROCESS | OPEN ACCESS

THE EMBO JOURNAL

Extracellular vesicles and co-isolated endogenous retroviruses from murine cancer cells differentially affect dendritic cells

Federico Cocozza[1,2], Lorena Martin-Jaular[1,3], Lien Lippens[4], Aurelie Di Cicco[5,6], Yago A Arribas[1], Nicolas Ansart[1], Florent Dingli[7], Michael Richard[7], Louise Merle[1], Mabel Jouve San Roman[8], Patrick Poullet[9], Damarys Loew[7], Daniel Lévy[5,6], An Hendrix[4], George Kassiotis[10], Alain Joliot[1], Mercedes Tkach[1,*,†] & Clotilde Théry[1,3,**,†]

Abstract

Cells secrete extracellular vesicles (EVs) and non-vesicular extracellular (nano)particles (NVEPs or ENPs) that may play a role in intercellular communication. Tumor-derived EVs have been proposed to induce immune priming of antigen presenting cells or to be immuno-suppressive agents. We suspect that such disparate functions are due to variable compositions in EV subtypes and ENPs. We aimed to characterize the array of secreted EVs and ENPs of murine tumor cell lines. Unexpectedly, we identified virus-like particles (VLPs) from endogenous murine leukemia virus in preparations of EVs produced by many tumor cells. We established a protocol to separate small EVs from VLPs and ENPs. We compared their protein composition and analyzed their functional interaction with target dendritic cells. ENPs were poorly captured and did not affect dendritic cells. Small EVs specifically induced dendritic cell death. A mixed large/dense EV/VLP preparation was most efficient to induce dendritic cell maturation and antigen presentation. Our results call for systematic re-evaluation of the respective proportions and functions of non-viral EVs and VLPs produced by murine tumors and their contribution to tumor progression.

Keywords antigen presenting cells; endogenous retrovirus; exosomes; extracellular vesicles; tumors

Subject Categories Cancer; Membranes & Trafficking; Microbiology, Virology & Host Pathogen Interaction

DOI 10.15252/embj.2023113590 | Received 23 January 2023 | Revised 31 October 2023 | Accepted 2 November 2023 | Published online 11 December 2023

The EMBO Journal (2023) 42: e113590

Introduction

Intercellular communication is crucial in all tissues, and especially in the tumor microenvironment, where cancer cells must instruct the surrounding stromal and immune cells to eventually form a tumor. Cells can interact with each other and with the extracellular medium through soluble secreted factors, but also through extracellular vesicles (EVs) and other non-vesicular extracellular nano-particles (NVEPs, shortened in ENPs here). In the last few years, the development of novel isolation and detection technologies of EVs have increased our knowledge on EVs/ENPs heterogeneity (Tkach *et al*, 2018; Willms *et al*, 2018) and highlighted the existence of novel subtypes of non-vesicular extracellular particles such as exomeres (Zhang *et al*, 2018), supermeres (Zhang *et al*, 2021b), and supramolecular attack particles (Balint *et al*, 2020). However, except for the latter which display killing activity, little is known still on the biological functions of these recently discovered particles (Zhang *et al*, 2019). In addition, most of the functional capacities attributed to EVs were observed with a mixture of EV subtypes (mixed endosome-derived exosomes and plasma membrane-derived ectosomes), ENPs and other components collectively considered as contaminants

1 INSERM U932, Institut Curie Centre de Recherche, PSL Research University, Paris, France
2 Université de Paris, Paris, France
3 Institut Curie Centre de Recherche, CurieCoreTech Extracellular Vesicles, Paris, France
4 Laboratory of Experimental Cancer Research, Department of Human Structure and Repair, Ghent University, and Cancer Research Institute Ghent, Ghent, Belgium
5 Institut Curie, PSL Research University, Sorbonne Université, CNRS UMR168, Laboratoire Physico-chimie Curie, Paris, France
6 Institut Curie, PSL Research University, CNRS UMR144, Cell and Tissue Imaging Facility (PICT-IBiSA), Paris, France
7 Institut Curie, PSL Research University, Centre de Recherche, CurieCoreTech Spectrométrie de Masse Protéomique, Paris, France
8 CNRS UMR3215, Institut Curie, PSL Research University, Paris, France
9 Institut Curie, Bioinformatics core facility (CUBIC), INSERM U900, PSL Research University, Mines Paris Tech, Paris, France
10 Retroviral Immunology, The Francis Crick Institute and Department of Medicine, Faculty of Medicine, Imperial College, London, UK
*Corresponding author. Tel: +33 186640859; E-mail: mercedes.tkach@gmail.com
**Corresponding author. Tel: +33 156246716; E-mail: clotilde.thery@curie.fr
†These authors contributed equally to this work as last co-authors

(soluble proteins, lipoproteins, etc.), raising the questions of the specific properties of each subtype of EV and ENP.

Viral infection brings an additional level of complexity to the vesicular secretome. Viruses depend on biological processes of the host cells to survive and to form viral particles. In particular, enveloped viruses are enclosed in a host cell-derived lipid bilayer which, for instance, in the case of HIV, uses the EV formation machinery to be formed (Gould *et al*, 2003; Booth *et al*, 2006). Therefore, as cell-derived lipid bilayer-enclosed particles devoid of autonomous capacity of replication, enveloped viruses can be considered as a subtype of EVs. In addition, infection by viruses also leads to production, together with the virus, of non-infectious particles containing viral components including capsid (called viral like particles, VLPs), and modifies the amount and composition of the endogenous EVs, which can then also include viral components (Nolte-'t Hoen *et al*, 2016; Martin-Jaular *et al*, 2021). Endogenous retroviruses (ERVs) represent a potential source of enveloped viral particles and of modified endogenous EVs. ERVs are inserted in the genome of higher organisms, but are not necessarily part of a pathologic process, since they are normally mutated or repressed and thus cannot form infectious viral particles (Kassiotis & Stoye, 2017). However, their infectivity can be restored in physiological or pathological conditions, for instance, in immunodeficient models or in mouse tumors (Young *et al*, 2012; Ottina *et al*, 2018).

In the tumor microenvironment, tumor cells promote changes in surrounding cells of the stroma and the immune system (Whiteside, 2008; Gajewski *et al*, 2013), in part through the action of EVs and ENPs (Han *et al*, 2019). However, the actual effects of EVs/ENPs released by tumor cells towards the immune system are controversial: there is evidence showing both immune response activation resulting from tumor antigen transfer, and conversely, immunosuppressive functions (Thery *et al*, 2009; Robbins & Morelli, 2014; Greening *et al*, 2015). This discrepancy could be due to the different isolation methods and conditions used in these studies, leading to different combinations of heterogenous EVs, ENPs and associated contaminants, each bearing their specific and sometimes antagonist functions.

Tumor-derived EVs (endogenous or by bio-engineering) can carry antigens from the producing cells, either native or as peptides presented in MHC-I complexes on the EV membrane, and transfer it to dendritic cells (DCs), leading to a T cell-mediated antitumor response and tumor rejection (Wolfers *et al*, 2001; Zeelenberg *et al*, 2008; Chulpanova *et al*, 2018). Immature DCs surveil the peripheral tissues and have a high uptake capacity. Once they have captured antigens and sensed the microenvironment, they can eventually mature and migrate to lymph nodes, especially if they have detected damage, pathogen or inflammatory molecules. There, they can activate or tolerize T cells, depending on the sensed signals (Banchereau & Steinman, 1998). In addition to containing antigens, it has been proposed that EVs possess an adjuvant-intrinsic effect due to the presence of damage-associate molecular patterns (DAMPs), which may explain why EVs are more efficient than soluble proteins at transferring antigens to antigen-presenting cells (APCs) (Morelli *et al*, 2004; Robbins & Morelli, 2014). However, whether the antigen transfer capacities or the DAMPs are carried by all EV subtypes or ENPs, or only some specific types is unknown.

Here, we have tackled this question by first characterizing the heterogeneity of EVs and ENPs isolated from the murine mammary tumor cell line EO771. Surprisingly, we found a remarkable amount of enveloped virus-like particles (VLPs), including some with infectious capacity, in our preparations, that we identified as produced from endogenous murine leukemia virus (MLV). Viral gag proteins and/or VLPs were also observed in 12 other tumor cell lines, but not in two lung carcinoma and one immortalized fibroblastic cell lines. We established a protocol to reliably separate the VLPs from other small EVs and ENPs. We characterized the tumor particle subtypes by quantitative proteomic analysis and analyzed their respective capacity to transfer antigen and activate dendritic cells *in vitro*. Unexpectedly, our results unravel a limited potential of VLP-devoid small EVs for the induction of antigen-specific immune responses. By contrast, a mixture of large/dense EVs and VLPs displayed the highest immune activation potential.

Results

EO771 cells secrete heterogenous particles including EVs, ENPs and VLPs into the extracellular medium

We chose the EO771 mouse cell line as a model of breast tumor cells that can be used for downstream analysis of antigen presentation in the syngeneic mouse C57BL/6 genetic background. To explore the heterogeneity of the EVs and particles secreted by EO771, we first performed a rough separation of large/medium EVs, small EVs and ENPs, based on classical differential centrifugation protocols (Thery *et al*, 2006; Jeppesen *et al*, 2019). Briefly, the serum-free conditioned medium depleted of dead cells and largest particles by a 2,000 *g* centrifugation was concentrated using 10 kDa filters, followed by sequential ultracentrifugation at 10,000 *g* (16 min), 200,000 *g* (50 min) and 200,000 *g* overnight (ON) to obtain pellets called 10k, 200k and ENPs, respectively (Fig 1A). Nanoparticle tracking analysis showed that, as expected, the 10k pellets contained more EVs larger than 200 nm in diameter than the 200k and ENPs (Fig EV1A). Of note, however, by NTA analysis, particles smaller than 50 nm could not be detected, and all pellets contained a majority of small EVs (< 200 nm in diameter).

The 10k, 200k and ENP pellets obtained from the same number of producing cells (20×10^6) were run on a western blot together with the lysate of the producing cells (2×10^5) and revealed with antibodies against transmembrane (CD9, CD63), external membrane-bound (milk-fat globule-EGF-factor VIII, MFGE8), and cytosolic proteins (Alix, Ago2, Hsp90) classically used to characterize EVs and/or ENPs (Fig 1B). The total protein stain showed that ENPs contained the highest amount of proteins, followed by the 200k and 10k. However, looking at specific markers, the 200k was enriched in CD63, CD9 and MFGE8, also found in the 10k but not in the ENPs. By contrast, Alix was only detected in the 200k. Conversely, Ago2 was mainly detected in the ENPs and, to a lesser extent, in the 200k. Finally, the full-length Hsp90 (*, Fig 1B) was found only in the cell lysate and the ENPs but not in the 10k or 200k, although a shorter band of around 70 kDa (Fig 1B) was detected in the latter, probably corresponding to a previously described stress-induced cleaved form (Beck *et al*, 2009).

Cryo-electron microscopy (cryo-EM) (Fig 1C) revealed a great heterogeneity of particles in the 10k and 200k, including vesicles of various sizes and aspects, as well as smaller particles (10–30 nm in

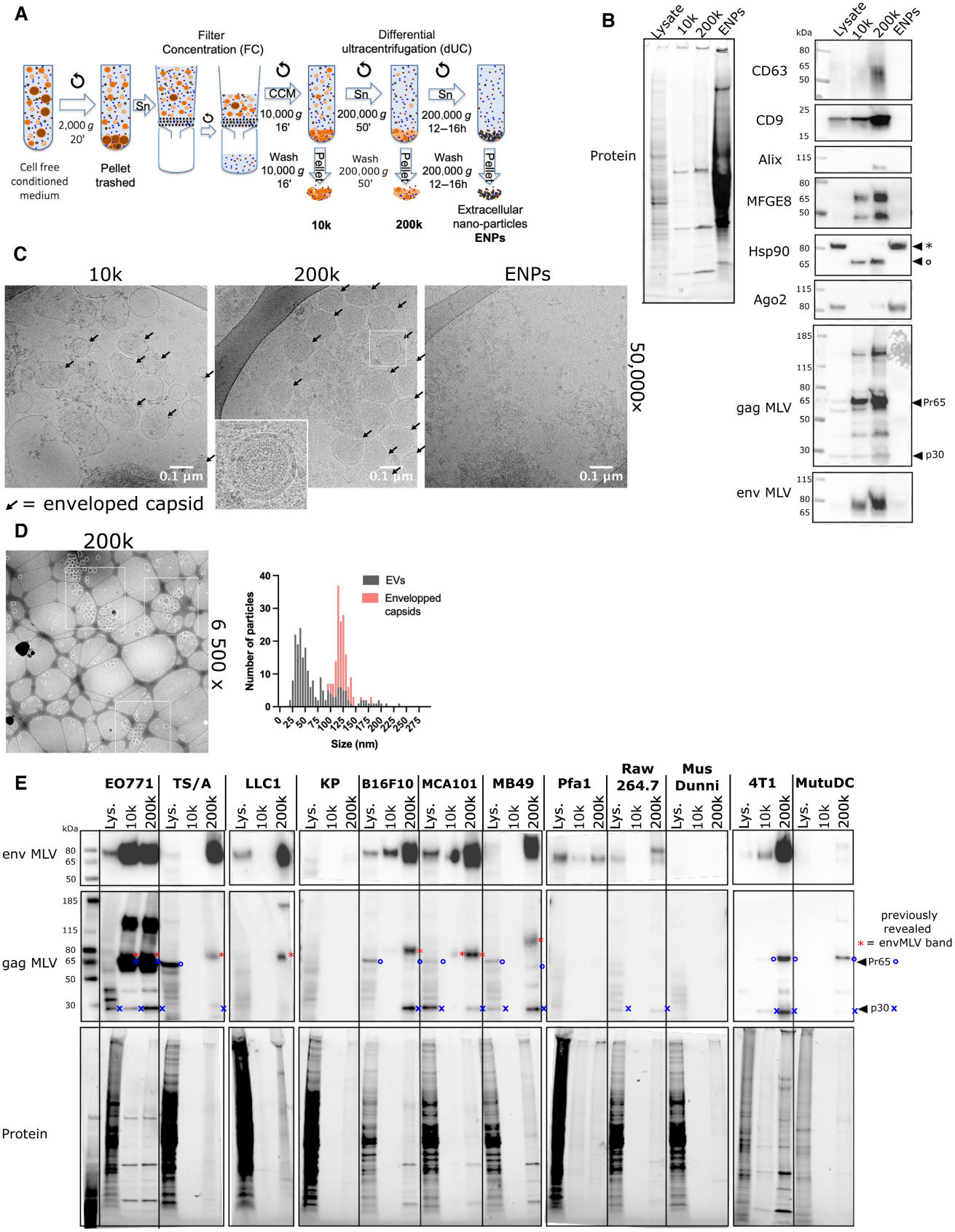
A
Filter Concentration (FC)
Differential ultracentrifugation (dUC)
2,000 g 20'
Sn
CCM 10,000 g 16'
200,000 g 50'
200,000 g 12–16h
Cell free conditioned medium
Pellet trashed
Wash 10,000 g 16'
Wash 200,000 g 50'
Wash 200,000 g 12–16h
Pellet
10k
200k
Extracellular nano-particles ENPs
B
Lysate
10k
200k
ENPs
Protein
kDa
CD63
CD9
Alix
MFGE8
Hsp90
Ago2
gag MLV
env MLV
Pr65
p30
C
10k
200k
ENPs
50,000×
0.1 µm
↙ = enveloped capsid
D
200k
6 500 x
EVs
Envelopped capsids
Number of particles
Size (nm)
E
EO771
TS/A
LLC1
KP
B16F10
MCA101
MB49
Pfa1
Raw 264.7
Mus Dunni
4T1
MutuDC
Lys.
10k
200k
env MLV
gag MLV
Protein
previously revealed
* = envMLV band
Pr65
p30

Figure 1.

Figure 1. Characterization of the EVs and ENPs from EO771 cell line: presence of virus-like particles (VLPs).

A Scheme of the protocol of separation of 10k, 200k and ENPs.

B Western blot showing total proteins (left) and various protein markers as indicated (right). Lysate from 2 × 10^5 EO771 cells, 10k, 200k and ENPs secreted by 20 × 10^6 EO771 cells were loaded on the gel. * indicates specific Hsp90 band of the expected size. ° indicates a shorter size band resulting from endogenous cleavage.

C Cryo-EM of EO771 10k, 200k and ENPs. Arrows indicate typical capsid-like structures inside EVs. One such structure highlighted by a white square is shown in a zoom (below, right).

D Quantification of size and presence ("enveloped capsids") or absence (EVs) of a VLP structure in all particles of one representative sample of 200k analyzed by cryo-EM (from the image at 6,500× magnification).

E Western blot of cell lysate (Lys) from 2 × 10^5 cells, 10k and 200k secreted by 20 × 10^6 of 10 tumor cell lines (EO771, TS/A, LLC1, KP, B16F10, MCA101, MB49, Raw264.7, 4T1 and MutuDC) and 2 non-tumoral fibroblast cell lines (Pfa1 and *Mus Dunni*), showing hybridization with antibodies against env (top) and gag (middle) viral proteins and total proteins (bottom). Gag is observed with different sizes, especially the full-length Pr65 (blue circle), and the mature cleaved p30 (blue cross) forms. Cell lysates of 5 additional cells (MC38, B3Z, EL4, EG7, splenocytes) are shown in Fig EV1C.

Source data are available online for this figure.

diameter) without any apparent lipid bilayer, and aggregates of electrodense material. ENPs contained mainly the latter two structures. Surprisingly, some of the vesicles in the 10k and 200k contained circular structures with regular concentric strips (arrows and close-up in Fig 1C), a shape typical of viral capsids (Qu *et al*, 2018), suggesting the presence of virus-like particles (VLPs). We quantified the size and the VLP aspect of the vesicles in the 200k (Fig 1D). VLP-shaped vesicles were concentrated in the range of 100–150 nm diameter (peak at 115–130 nm), consistent with the observed size of *in vitro* reconstituted murine leukemia virus (MLV) (Qu *et al*, 2018), but were never observed among smaller vesicles (25–60 up to 80 nm diameter).

To determine whether these particles were actually of viral origin, we performed a qualitative mass spectrometry-based proteomic analysis of the 200k. Mass spectrometry files were interrogated, to identify peptides from these proteins, against a data base containing the mouse proteome concatenated to protein sequences from all known mouse viruses (523 sequences manually extracted from Swissprot) and from 53 sequences of endogenous MLV envelope glycoproteins translated from the nucleotide sequences of proviruses annotated as previously described (Attig *et al*, 2017) (Fig EV1B, Dataset EV1). We detected several proteins of the family of murine leukemia virus (MLV), both exogenous (AKV, Duplan) and endogenous (Xmv, Intracisternal A-particle).

The western blot (Fig 1B) was thus further probed with antibodies against gag and envelope (env) proteins from MLV (R187 and 83A25 antibodies), which revealed the presence of both proteins in the 200k, and the 10k, but not in the ENPs. To determine whether this was a EO771 cell line-specific observation, we analyzed 13 additional mouse tumor cell lines of different genetic backgrounds and tissue origins, 2 non-tumoral fibroblast cell lines (Pfa1 and *Mus Dunni*), and primary splenocytes, for expression of gag and env in cell lysates (Fig EV1C) and/or 10k and 200k pellets (Figs 1E and EV1B). The env protein was detected in all cells and their EV pellets by western blot and/or proteomic, except in the KP lung carcinoma cell, the *Mus Dunni* cell line and primary splenocytes. Gag was not expressed in the 3 cells that did not express env, nor in 2 cells that expressed env: LLC1 and Pfa1 (Figs 1E and EV1C). All the other cells (12/17) expressed various levels of either full-length (Pr65) or matured (p30) gag, especially in the 200k pellets. VLP structures were also observed by cryo-EM in 200k pellets of the tumor dendritic cell line MutuDC (Fig EV1D).

Finally, we evaluated the infectivity capacity of these viral particles by exposing permissive *Mus Dunni*-XG7 cells (where a GFP-encoding reporter provirus is mobilized upon retroviral infection) to the 200k of EO771 for 24 h. The cell-conditioned medium (CCM) was then collected once per week during 2 weeks, and the last CCM was added to unmodified *Mus Dunni* (Young *et al*, 2012): detection of GFP-expressing cells in the CCM-exposed *Mus Dunni* cells confirmed the presence of infectious retroviral particles in the 200k of EO771 and of MutuDCs (Fig EV1E). Therefore, the VLP preparations also contained infectious retroviruses. However, not knowing the proportions of infectious viruses and defective virus-like particles, we chose to use the term VLP as a generic name for both fully functional and defective viruses in the rest of the results section.

sEVs and VLPs can be separated through a velocity gradient

Because the protocol of separation shown in Fig 1A resulted in a mix of EVs and VLPs in the 10k and 200k, we next tried to separate VLPs from the other EVs. We used EVs from EO771, as this cell line, among all the tested cells, released most abundantly gag and env proteins (Fig 1E). We first used asymmetric flow field-flow fractionation (AF4), which had been previously successfully implemented to separate exomeres (also called ENPs) and two types of EVs, respectively of 60–80 and 90–120 nm of diameter (Zhang *et al*, 2018). Using settings shown in Fig EV2A, we managed to separate from 200k pellets of EO771 small protein-rich structures (Fig EV2B and D: P2) from light-scattering EVs, among which we recovered three populations of 35–80 nm (P3), 80–180 nm (P4) and 180–220 nm (P5) diameters (Fig EV2B–D). However, this method did not separate VLPs from small EVs of the same size, since both were identified by cryo-EM in the P4 and the P5 EV-containing AF4 fractions of the 200k pellets (Fig EV2D).

We then refined the ultracentrifugation protocol by adding an additional step of velocity gradient. We loaded the 10k (Fig EV3) or 200k (Fig 2) from EO771 cells on top of an iodixanol density gradient and centrifuged for a short time (1 h30), adapting a protocol previously performed to separate HIV-1 virus from other EVs (Cantin *et al*, 2008; Liao *et al*, 2019; Martin-Jaular *et al*, 2021). After measuring their density (Fig 2A), we washed eight fractions of 2 ml each (1 to 8, top-to-bottom) by ultracentrifugation, resuspended them in PBS and processed for NTA measurements (Fig 2B) and western blot analysis (Fig 2C and D). Two peaks of particles were observed from the 200k, in fractions 2–3 and in fractions 5–6 (Fig 2B), while from the 10k, a single peak of particles was observed in the denser part, fractions 5–6 (Fig EV3A). The total protein stain

of the 200k fractions showed distinct patterns of proteins in fractions 1–3 and 5–8 (Figs 2C and EV3B). Remarkably, 3 prominent bands were detected in the denser fractions (5–8) but absent in the low-density fractions (1–3). We then probed the western blot with an antibody against gag of MLV (Figs 2D and EV3B), revealing several bands in fractions 5–8, 2 of which likely corresponded to the prominent proteins (around 65 and 30 kDa, * and ° in Fig 2C). The env MLV protein was also enriched in fractions 5–7, displaying different size variants, but it was also found in fractions 2–3 (Figs 2D and EV3B). The EV markers were distributed along the 8 fractions with different abundances depending on the marker (Fig 2D). While CD9, MFGE8 and Alix were equally present in fractions 1–3 and 5–8, CD63 and Ago2 were mostly in fractions 1–3, whereas MHC-I and the short band recognized by anti-Hsp90 (° in Fig 2E, Hsp90 panel) were most prominently detected in fractions 5–7. Cryo-EM analysis (Fig 2E) confirmed that a vast majority of capsid-containing structures constituted the 5–7 fractions, while hardly any were visible in the 1–3 fractions. These results show that fractions 1 to 3 from the velocity gradient-based separation of 200k contained mainly endogenous and virus-modified sEVs, while fractions 5–8 contained VLPs. Fraction 4 consisted in a mixture of both. ENPs were not present in any of the fractions, probably because the few ENPs present in the 200k (pelleted after 50 min rather than ON) were lost during the fraction washing step also performed for 50 min. By contrast, the velocity gradient was not effective to separate the EVs from the VLPs in the 10k pellets, since all the particles were recovered in fractions 5–7 (Fig EV3A and B). Velocity gradient applied to 200k from Pfa1 cells showed the absence of the prominent bands and gag-labeled proteins in fractions 5–8, confirming that these cells do not release VLPs (Fig EV3C).

Thus, using a pipeline of combined protocols (Fig 2F), we separated three different types of particles or vesicles: sEVs (200k velocity gradient fractions 1–3), VLPs (200k velocity gradient fractions 5–7), and ENPs (200,000 *g* ON pellet of the supernatant of 200,000 *g* 50 min, Figs 1A and 2F). Additionally, we isolated two different mixtures of EVs and/or ENPs (Fig 2F): the 10k pellet containing large/dense EVs plus VLPs (10k), and a mixture of all the remaining particles pelleted by ultracentrifugation at 200,000 *g* ON of the supernatant of the 10,000 *g* centrifugation (Mix). This new "Mix" sample was included in the following experiments, as representative of an heterogenous mixture of particles physiologically secreted by tumor cells. We systematically recovered these five sample types (10k, sEVs, VLPs, ENPs, Mix) from each batch of EO771-conditioned medium, in several independent experiments. We quantified the number of particles by nanoparticle tracking analysis (NTA) (Fig EV3D, left) and the amount of proteins recovered in each sample (Fig EV3D, right). The Mix fraction was the most enriched in particles, while ENPs were the least enriched. By contrast, the amount of proteins was the highest in the ENPs and in the Mix. Analyzed by NTA, the 10k had a significantly larger median size than sEVs and ENPs (Fig EV3E, left), but not significantly different from that of VLPs. The zeta potential of ENPs was significantly less negative than that of all EVs types (Fig EV3E, right). Finally, only 10k and VLP preparations, but neither sEVs, nor ENPs or Mix, induced dose-dependent exposure of env protein on the surface of target *Mus Dunni* cells after 24 h of culture (Fig EV3F), suggesting that only VLPs and 10k contained infectious retroviral particles, or at least enough env to transfer it to target cells.

Quantitative proteomic analysis of the different particle subtypes

We next performed a quantitative proteomic analysis by label-free mass spectrometry on 10k, sEVs, VLPs, ENPs and Mix samples from EO771, adjusted to the same amount of proteins. Proteins were identified combining the databases of mouse and murine virus proteins as in Fig EV1B. 6,127 proteins in total, including 53 viral proteins, were identified by at least three peptides among five replicates in at least one type of sample (Dataset EV2: Venn Diagram tab). Venn diagram analysis showed that most of the identified proteins (3,800 total, including 35 viral proteins) were shared between all groups (Fig 3A, with Mix sample excluded from the Venn Diagram analysis for better visualization of the single fraction-specific components). Nevertheless, 303 proteins (including 4 viral) were found only in the 10k, 130 (including 1 viral) in the sEVs, 63 in the VLPs and 231 in the ENPs (Dataset EV2: Venn Diagram tab). Principal Component analysis (PCA) of the label-free quantification (LFQ) results (Dataset EV2: LFQ), showed clustering of the five replicates of each fraction (Fig 3B, and heatmap of protein abundance: Fig EV4A), confirming the reproducibility of our protocol. ENPs and the Mix were tightly close, indicating the prevalence of ENPs in the latter. Both were far from the membrane-containing 10k, EVs and VLPs, although to a lesser extent for the Mix, in agreement with the heterogeneous composition of this fraction which contains sEVs, VLPs and ENPs. Because of this mixed composition, the Mix was excluded from further analyses, since we aimed at identifying specific protein signatures of EV subtypes.

A Gene Ontology (GO)-term enrichment analysis was performed, first on the top-100 most abundant proteins of each group (i.e. including the shared abundant proteins) (Fig EV4B). The most significantly enriched "cellular component" GO-terms found in all samples were focal adhesion and cell-substrate junction, suggesting that areas of cell interaction with each other and with their substrate were major sources of EVs/ENPs. Other enriched GO-terms included ribosome- and nucleus-related terms, which were especially significantly enriched in sEVs and in ENPs, while terms corresponding to lumen of various internal compartments (including ficolin-1-containing compartments) were more enriched in 10k and VLPs.

We next used the state-specific protein analysis (SSPA) feature of the myProMS software (as described in Materials and Methods) to identify proteins specific to or significantly enriched in one or a group of samples (Dataset EV2: SSPA tab). GO-term enrichment analysis on the top-100 most enriched specific proteins of the 10k highlighted membranes of mitochondria, ER and secretory granules. The top-100 proteins of ENPs were enriched in GO-terms for lumen of secretory granules and lysosomes, as well as membrane of secretory and coated vesicles. sEVs top-100 proteins were enriched in nuclear components as well as both lumen and membrane components of organelles. Given the low number of specific proteins in VLPs (see Fig 3A and D), only 3 significantly enriched GO-terms were identified: trans-Golgi network, and two complexes involved in regulation of transcription and histone modification (the STAGA and the SAGA complexes) (Fig 3C). Abundance of the 15 most specifically enriched proteins of each sample type (only 10 for VLPs) is shown in Fig 3D.

Finally, when we focused the analysis on the identified viral proteins (Dataset EV2), the majority of peptides matched with MLV

proteins as identified by a few proteo-specific peptides: AKV, Duplan, but also endogenous MLV (MLV-chr5). Other viruses identified by more than one specific peptide included intracisternal a-particle, and, in lower amounts, Cas-Br-E MLV, Xmv41, lymphocytic choriomeningitis virus, murid herpes virus, mengo encephalomyocardiatis virus and murine coronavirus. The SSPA

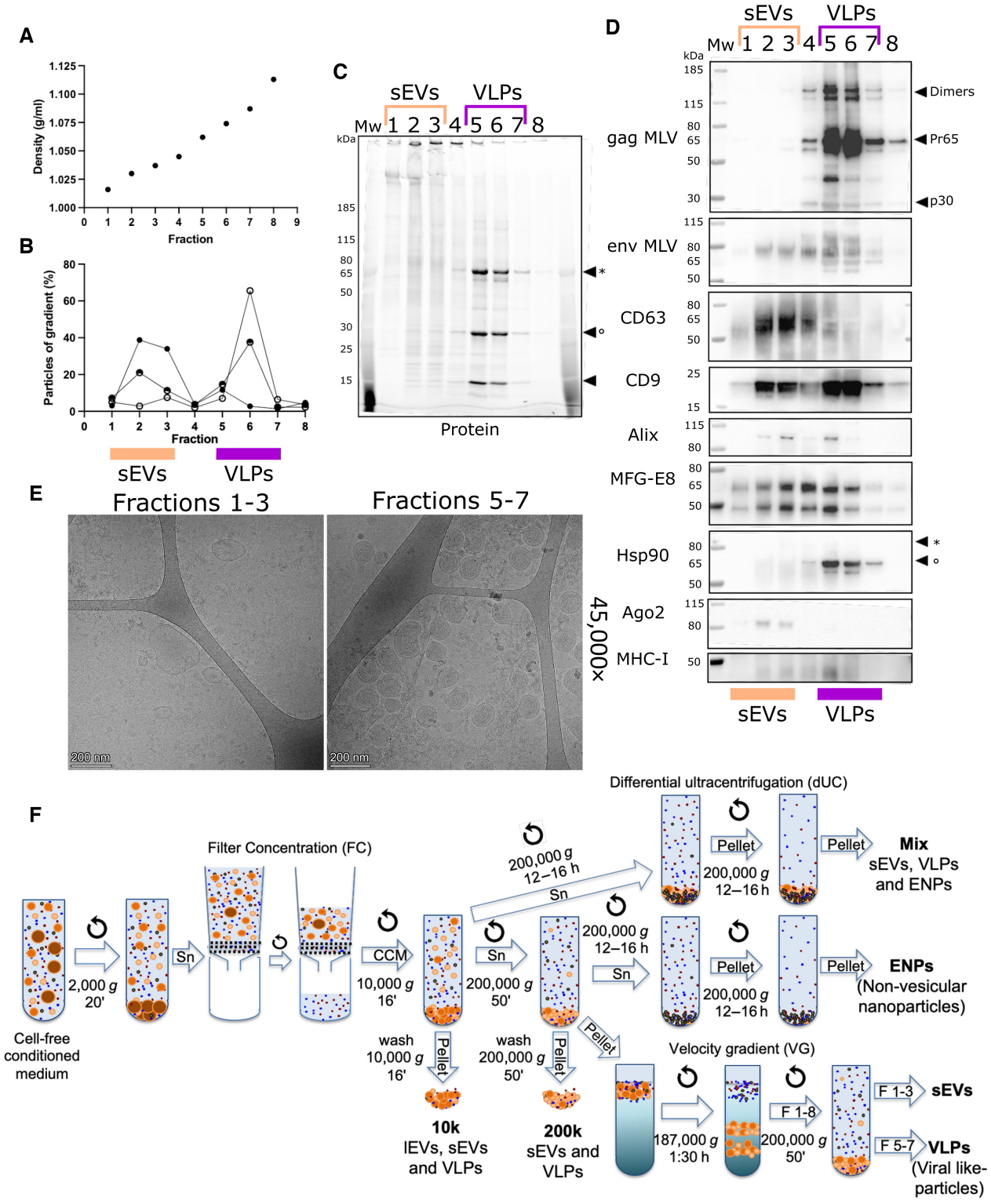

Figure 2.

Figure 2. Separation of sEVs and VLPs present in the 200k pellet.

A Density of fractions of 2 ml (1–8) of the velocity gradient.

B Percentage of number of particles in each fraction over the total measured for all the gradient. Each line corresponds to an independent experiment. $n = 3$.

C Protein stain-free image of a representative gel of fractions 1–8 from the gradient. * ° = prominent bands in fractions 5–7 of the same size as Pr65 and p30 gag bands in 2D.

D Representative western blot stained with antibodies against MLV, EV and ENP markers. * ° in Hsp90 = position of full-length and short bands as observed in the 10k and 200k of Fig 1B.

E Cryo-EM of fractions 1–3 (sEVs) and fractions 5–7 (VLPs) from EO771.

F Summary of the combined protocols used to recover 10k, 200k, sEVs, VLPs, ENPs and Mix.

Source data are available online for this figure.

(Dataset EV2, Fig 3E) showed that gag-pol and pol proteins were generally enriched in both the 10k and VLPs as compared to sEVs and ENPs. The envelope proteins, by contrast, were variably distributed in all fractions. These distributions, therefore, confirmed the western blot analyses (Figs 1B and 2D and EV3B). A few other viral proteins were detected, although at low levels, in sEVs and ENPs: the RNA polymerase L of the sendai and the lymphocytic choriomeningitis virus, or the replicase of coronavirus, suggesting that elements of other viruses can end up in sEVs.

Tumor derived EVs and particles induce distinct phenotypic changes in DCs

Given the different protein composition of each type of particles, we hypothesized that they may induce different effects on target cells. Due to our primary interest for the role of tumor-derived EVs in establishment of antigen-specific immune responses, we chose canonical antigen presenting cells, dendritic cells (DCs), as targets of tumor-derived EVs for the subsequent functional studies (Fig 4A). The same amount of proteins (10 or 20 μg/ml final, Fig 4B, or a dose response of $0.5–4 \times 10^{10}$ particles/ml corresponding to 2–2,000 μg/ml final, Figs 4C and EV5A) of each of the particle fractions isolated from EO771 as described in Fig 2F were added for 16 h to MutuDC, a model cDC1 cell line from C57BL/6 (Fuertes Marraco *et al*, 2012). Then, we measured MutuDC cell viability and surface expression of maturation markers by flow cytometry (Fig 4A–G, gating strategy in Appendix Fig S1A), and we quantified cytokine release in the supernatant by cytokine-bead array (CBA) (Fig 4H).

Remarkably, purified sEVs induced the death of MutuDC (Fig 4B and C). This toxicity was not due to insufficient washing of the iodixanol from the fractions 1–3, since it was not observed with the higher density iodixanol gradient fraction VLPs, while the 200k, containing sEVs and VLPs but devoid of any iodixanol, also induced death (Fig 4B). We observed a very limited cytotoxic effect induced by the 10k, VLPs, or ENPs, and a low death inducing ability of Mix, probably due to the dilution of sEVs by VLPs and ENPs in this sample. Diluting sEVs with VLPs at increasing ratio (Fig 4D) reduced the toxicity of sEVs, in a manner suggesting dilution of the effect, rather than inhibition of sEVs' activity by VLPs. Finally, this cytotoxicity was not observed at all when using EVs and particles isolated from the non-tumor cell line Pfa1 (Fig 4B), whereas it was observed when using 200k pellets from tumor cells B16F10 or LLC1, but not from MCA101 nor KP (Fig 4E).

To confirm these results in a more physiological context, the EO771-derived particle treatments were applied to primary DCs isolated from the spleen of a C57BL/6 mouse (Fig EV5B, gating strategy in Appendix Fig S1B and C). Basal viability of isolated DCs after 16 h of culture was low (PBS condition in Fig EV5B): 20–30% for the global DC population, with a better survival of cDC2 (60% viability). Treatment by sEVs (but not by any other samples) further decreased the viability to 10% for the global population and to 20% for cDC2. The low survival rate of pDC (20%) was decreased to 10% by treatment with any vesicle-containing samples (10k, VLPs, sEVs, Mix), but not by treatment with ENPs. Finally, the death-inducing ability of sEV was not species-specific, as it was also observed on primary DCs generated from human monocytes (Fig EV5C, gating strategy in Appendix Fig S1D).

We then asked how EV/ENP subtypes changed the maturation profile of MutuDCs (Figs 4F and G, and EV5D and E, gating strategy in Appendix Fig S1A). CpG and LPS were used as internal control of DCs' ability to respond to maturation-inducing signals. Treatment by the EO771 10k pellets significantly increased expression of CD40 (Fig 4F) and MHC-II and, to a lower (and not significant) extent, of CD86 and PD-L1 (Fig EV5D). Treatment by sEVs, VLPs and 200k only slightly increased expression of CD40 and MHC-II, whereas ENPs did not induce increase of any of these markers (Figs 4F and EV5D). MutuDC did not overexpress any of the analyzed co-stimulatory molecules when exposed to the Pfa1 EVs or particles (Fig 4F), while they upregulated CD40 and the other markers when exposed to 10k and (to a lower extent) 200k pellets of the 4 other mouse tumor cell lines B16F10, MCA101, LLC1, KP (Figs 4G and EV5E).

A panel of 17 cytokines were next quantified in the conditioned medium of MutuDC. Eight of these cytokines were detected in at least one of our samples (Fig 4H). Three of them were also detected in the EVs and ENPs that had been used for treatment of MutuDC (bottom panel Fig 4H): in particular, MCP1 was abundant in ENPs and also present in the other particles, while RANTES and IL10 were detected in all types of EVs and in ENPs but at a very low level. Therefore, MCP1 detected in the supernatant of all EV-treated MutuDC was possibly coming from the EVs rather than from the cells and will not be discussed further. The 10k pellet was the most efficient to induce cytokine secretion by MutuDC, which released the 7 cytokines at a higher level than control (untreated) MutuDCs: 3 for which the difference with control treatment was statistically significant (IL6, MIP1a, MIG), 2 which were not statistically different from control but still expressed at a much higher level (TNFa, MIP1b), and 2 expressed at a low level (IL10, RANTES). The second most efficient treatment was sEVs, which induced statistically significant increased secretion of MIG and non-statistically significant (but still higher than control) levels of IL6, TNFa, MIP1b, MIP1a,

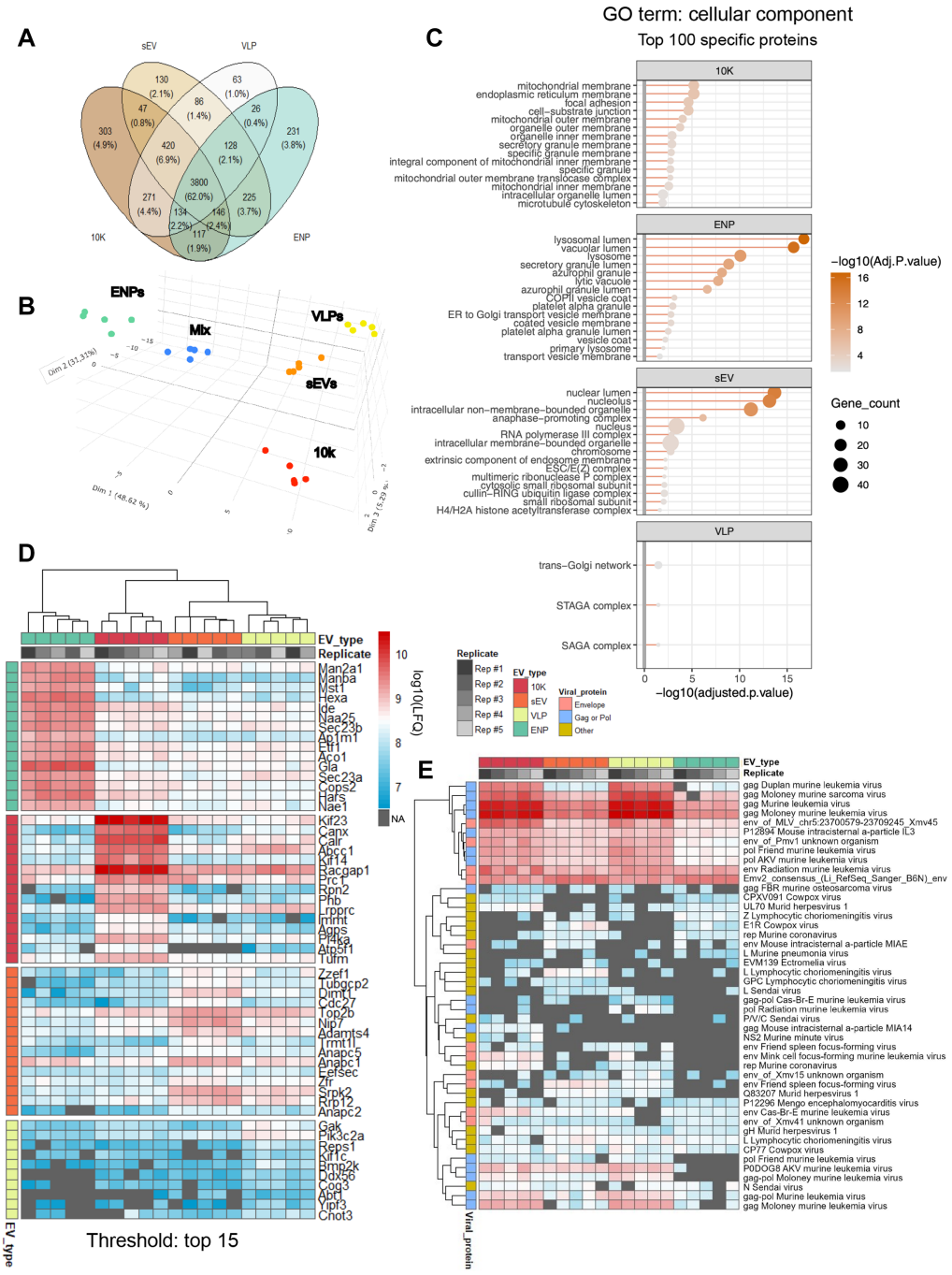

Figure 3. Proteomic characterization of subtypes of particles.

A Venn diagram of all (mouse + viral) proteins identified with at least three peptides among five biological replicates in at least one sample type among the 10k, sEVs, VLPs and ENPs. All proteins are listed in Dataset EV2, VennDiagram table.

B 3D view of the first three components of the principal component analysis (PCA) of all samples based on their protein abundance (LFQ). Samples are colored by subtypes: 10k = red; sEVs = orange, VLPs = yellow, ENPs = green, Mix = blue.

C GO term-enrichment analysis for cellular components in the top-100 most specific proteins (from Dataset EV2, SSPA tab): the only 3 significant GO-terms (for VLPs) or the 15 most significant GO-terms (for 10k, sEVs and ENPs) are shown. GO-terms are ordered by adjusted *P*-value. Statistical analysis was performed using the default parameters of Enrichr package.

D Heatmap of protein abundance of the 15 most specific proteins (or the only 10 specific proteins for VLPs) of each group (from SSPA analysis, Dataset EV2). Clustering is shown to confirm that specific proteins are not identified due to outlier replicates. NA = not detected/absent.

E Heatmap of protein abundance of the 46 quantified viral proteins in the different fractions. All gag-pol sequences are primarily present in the 10k and VLPs, whereas envelope proteins (env) are more equally distributed between the fractions. NA = not detected/absent.

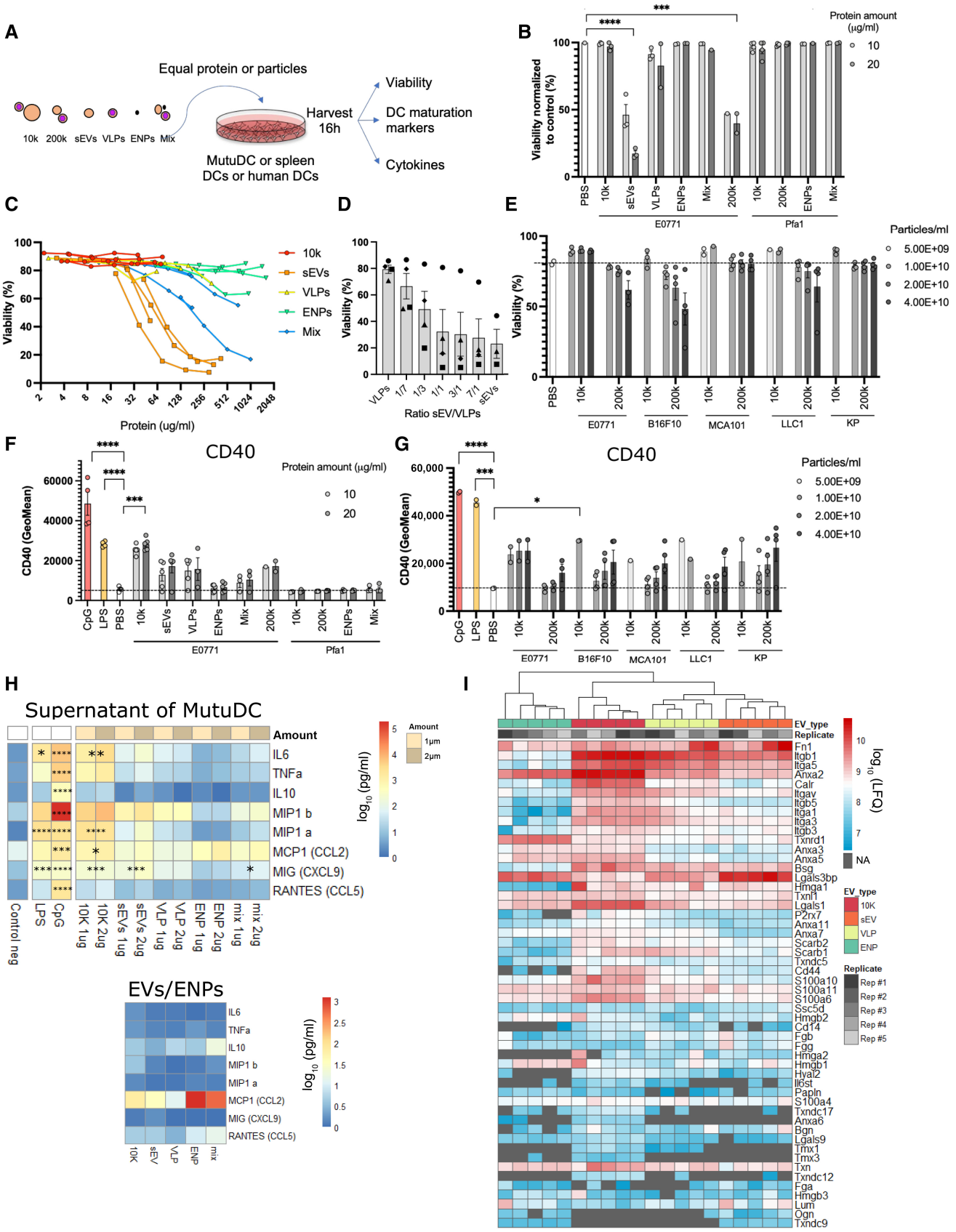
A
Equal protein or particles
10k 200k sEVs VLPs ENPs Mix
MutuDC or spleen DCs or human DCs
Harvest 16h
Viability
DC maturation markers
Cytokines
B
Protein amount (µg/ml)
10
20
Viability normalized to control (%)
PBS 10k sEVs VLPs ENPs Mix 200k 10k 200k ENPs Mix
E0771
Pfa1
C
10k
sEVs
VLPs
ENPs
Mix
Viability (%)
Protein (ug/ml)
D
Viability (%)
VLPs 1/7 1/3 1/1 3/1 7/1 sEVs
Ratio sEV/VLPs
E
Particles/ml
5.00E+09
1.00E+10
2.00E+10
4.00E+10
Viability (%)
PBS 10k 200k 10k 200k 10k 200k 10k 200k 10k 200k
E0771 B16F10 MCA101 LLC1 KP
F
CD40
Protein amount (µg/ml)
10
20
CD40 (GeoMean)
CpG LPS PBS 10k sEVs VLPs ENPs Mix 200k 10k 200k ENPs Mix
E0771
Pfa1
G
CD40
Particles/ml
5.00E+09
1.00E+10
2.00E+10
4.00E+10
CD40 (GeoMean)
CpG LPS PBS 10k 200k 10k 200k 10k 200k 10k 200k 10k 200k
E0771 B16F10 MCA101 LLC1 KP
H
Supernatant of MutuDC
Amount
1µm
2µm
IL6
TNFa
IL10
MIP1 b
MIP1 a
MCP1 (CCL2)
MIG (CXCL9)
RANTES (CCL5)
log10 (pg/ml)
Control neg LPS CpG 10K 1ug 10K 2ug sEVs 1ug sEVs 2ug VLP 1ug VLP 2ug ENP 1ug ENP 2ug mix 1ug mix 2ug
EVs/ENPs
IL6
TNFa
IL10
MIP1 b
MIP1 a
MCP1 (CCL2)
MIG (CXCL9)
RANTES (CCL5)
log10 (pg/ml)
10K sEV VLP ENP mix
I
EV_type
Replicate
log10 (LFQ)
NA
EV_type
10K
sEV
VLP
ENP
Replicate
Rep #1
Rep #2
Rep #3
Rep #4
Rep #5
Fn1
Itgb1
Itga5
Anxa2
Calr
Itgav
Itgb5
Itga1
Itga3
Itgb3
Txnrd1
Anxa3
Anxa5
Bsg
Lgals3bp
Hmga1
Txnl1
Lgals1
P2rx7
Anxa11
Anxa7
Scarb2
Scarb1
Txndc5
Cd44
S100a10
S100a11
S100a6
Ssc5d
Hmgb2
Cd14
Fgb
Fgg
Hmga2
Hmgb1
Hyal2
Ilo5t
Papln
S100a4
Txndc17
Anxa6
Bgn
Lgals9
Tmx1
Tmx3
Txn
Txndc12
Fga
Hmgb3
Lum
Ogn
Txndc9

Figure 4.

Figure 4. Phenotypic changes induced by the different subtypes of particles on MutuDC cells.

A Scheme of the *in vitro* experiment and the parameters assessed.

B Viability of MutuDC after 16 h of exposure to 10 or 20 μg/ml of the different particles coming from EO771 or Pfa1, measured by flow cytometry with eFluor 780 fixable viability dye (Appendix Fig S1A), normalized to the control non-treated condition. $n = 3$.

C Viability of MutuDC after 16 h of exposure to 0.5, 1, 2 and 4 × 10^{10} particles/ml of the different particles coming from EO771 cells, graphed in function of their corresponding concentration of protein. Graph in function of the particle concentration is shown in Fig EV5A. $n = 4$.

D Viability of MutuDC cells after 16 h of exposure to different ratios (1/7, 1/3, 1/1, 3/1, 7/1 and 1/0) of the mixture between sEVs and VLPs reaching 4 × 10^{10} particles/ml. $n = 4$.

E Viability of MutuDC after 16 h of exposure to 0.5, 1, 2 and 4 × 10^{10} particles/ml of 10k and 200k coming from a panel of tumor cell lines, 3 carrying MLV gag and env in their EVs (EO771, B16F10 and MCA101), 1 carrying only env (LLC1) and 1 carrying none (KP). $n = 2$–4.

F Expression of maturation markers on viable MutuDC cells after 16 h of exposure to 10 or 20 μg/ml of the different particles coming from EO771 and Pfa1, measured by flow cytometry (Appendix Fig S1A, GeoMean). LPS and CpG treatments were used as positive controls of maturation. $n = 5$.

G Expression of maturation markers on viable MutuDC cells after 16 h of exposure to 0.5, 1, 2 and 4 × 10^{10} particles/ml of the 10k and 200k coming from the same cells lines as in E. $n = 3$–4.

H Quantification of cytokines secreted by DCs in the supernatant of MutuDC exposed to the subtype of particles (top) and in the particles themselves (bottom), presented as heatmap (log10 scale). "Amount 1 μg/2 μg" refers to the amount of EV/ENP used to treat MutuDC (in 100 μl final volume). $n = 3$. Statistical analyses were performed using mixed-effects model with Dunnett's multiple comparison to the PBS, the mean of both concentrations was used for the comparisons, with different concentrations as repeated measures (B, F–H). n = number of biological replicates, i.e. independent EV production and subtype separation from the respective producing cells (B–H). Error bars = SEM (B, D–G). *$P < 0.05$, **$P < 0.01$, ***$P < 0.001$ and ****$P < 0.0001$ (B, F–H).

I Heatmap of protein abundance of proteins qualifying as DAMPs and PAMPs as quantified by LFQ in our proteomic analysis of the different types of particles (Dataset EV2). NA = not detected/absent.

Source data are available online for this figure.

RANTES. However, given the high rate of cell death observed in these cultures, some of these cytokines could have been induced by the detection of cell death rather than by direct signaling induced by sEVs. VLPs induced some IL6, MIP1b and MCP1, and even smaller amounts of TNFa and MIP1a. The only cytokine detected in ENP-treated DCs was MCP1, probably coming from ENPs themselves.

In conclusion, the 10k was the most inflammatory treatment, triggering the maturation of MutuDC and the secretion of several pro-inflammatory cytokines and chemokines, whereas ENPs did not have any effect on MutuDCs, VLPs induced low levels of DC maturation, and sEVs induced some maturation and cytokine secretion, but also significant cell death. Consistent with this observation, our quantitative proteomic data showed that proteins qualifying as DAMPs and PAMPs (according to a list defined as such in (Hoshino *et al*, 2020)) were most abundant in the 10k pellet (Fig 4I).

Membrane-containing particles 10k, sEVs and VLPs, but not ENPs can transfer protein effectively to DCs

A proposed mode of action of EVs is to deliver their content into target cells following their uptake. We thus wanted to compare the capacities of uptake of each of the EVs and particle subtypes. We chose the fluorescent protein mCherry as cargo of EVs/ENPs, as it is amenable to visualization and quantification by fluorescence microscopy, flow cytometry and spectroscopy. To induce its loading into EVs/ENPs, we introduced a myristoylation and a palmitoylation sequence upstream of mCherry to generate the myr/palm-mCherry (Fig 5A) (Valenzuela & Perez, 2020; Mathieu *et al*, 2021). In the resulting protein, post-translational addition of the acyl chains that insert into the cytosolic side of the lipid bilayer should lead to association of the fluorescent protein with internal membranes or lipidic structures (McCabe & Berthiaume, 1999, 2001) (Fig 5A), resulting in the targeting of this membrane-bound mCherry inside the released EVs and possibly in/on ENPs.

We transfected EO771 with a myr/palm-mCherry-expressing plasmid and we sorted mCherry$^+$ cells by flow cytometry to generate a stable cell line. We checked the cellular localization of the mCherry in the cells by confocal microscopy (Fig 5B). The mCherry fluorescence was found mainly at the plasma membrane of the cells but also internally, colocalizing partially with both CD9 and CD63.

To determine the targeting of the mCherry into the particle subtypes, the same western blot from Figs 1 and 2 (which contained EV/ENP samples from myr/palm-mCherry EO771) was revealed with an antibody against mCherry (Fig 5C): bands around 30 kDa, 26 and 24 kDa were detected in all particles as well as in all gradient fractions, although at different ratios. mCherry was also detected in the ENPs, mainly as the lower band form. Transmission EM analysis following immuno-labeling with anti-mCherry showed staining mostly associated to vesicles in the 10k and 200k pellets, with very few gold particles outside EVs, while most of the staining was associated with non-vesicular electron-dense structures in the ENP pellets (Fig 5D). This staining was specific since no gold particles were observed when 10k or ENP from non-mCherry-expressing cells were analyzed (Appendix Fig S2A). mCherry fluorescence was measured in each sample and compared to a standard curve of recombinant mCherry to quantify the absolute amount of mCherry. Since mCherry amount was not linearly correlated with the number of detected particles (Appendix Fig S2B), we chose for each type of sample to use the same amount of mCherry as quantified by fluorescence, rather than the same particle number or protein amount, to feed target cells and measure efficacy of uptake.

When exposed for 16 h to 10 or 30 ng of EV/ENP-associated mCherry or recombinant mCherry (rec mCherry), and analyzed by flow cytometry for mCherry fluorescence (gating strategy in Appendix Fig S1A), MutuDCs were observed to incorporate fluorescence from the 10k, sEVs, VLPs and Mix similarly and in a dose-dependent manner, but not from the ENPs (Fig 5E, left). Addition of a 100-fold excess of recombinant protein (2,500 ng, Fig 5E, right) was required to achieve the same degree of uptake observed with 30 ng of EV-associated mCherry.

We next performed the uptake assay with primary spleen DCs, which were exposed to 30 ng of EV/ENP-associated mCherry (Fig 5F, gating strategy in Appendix Fig S1B and C). In all DC

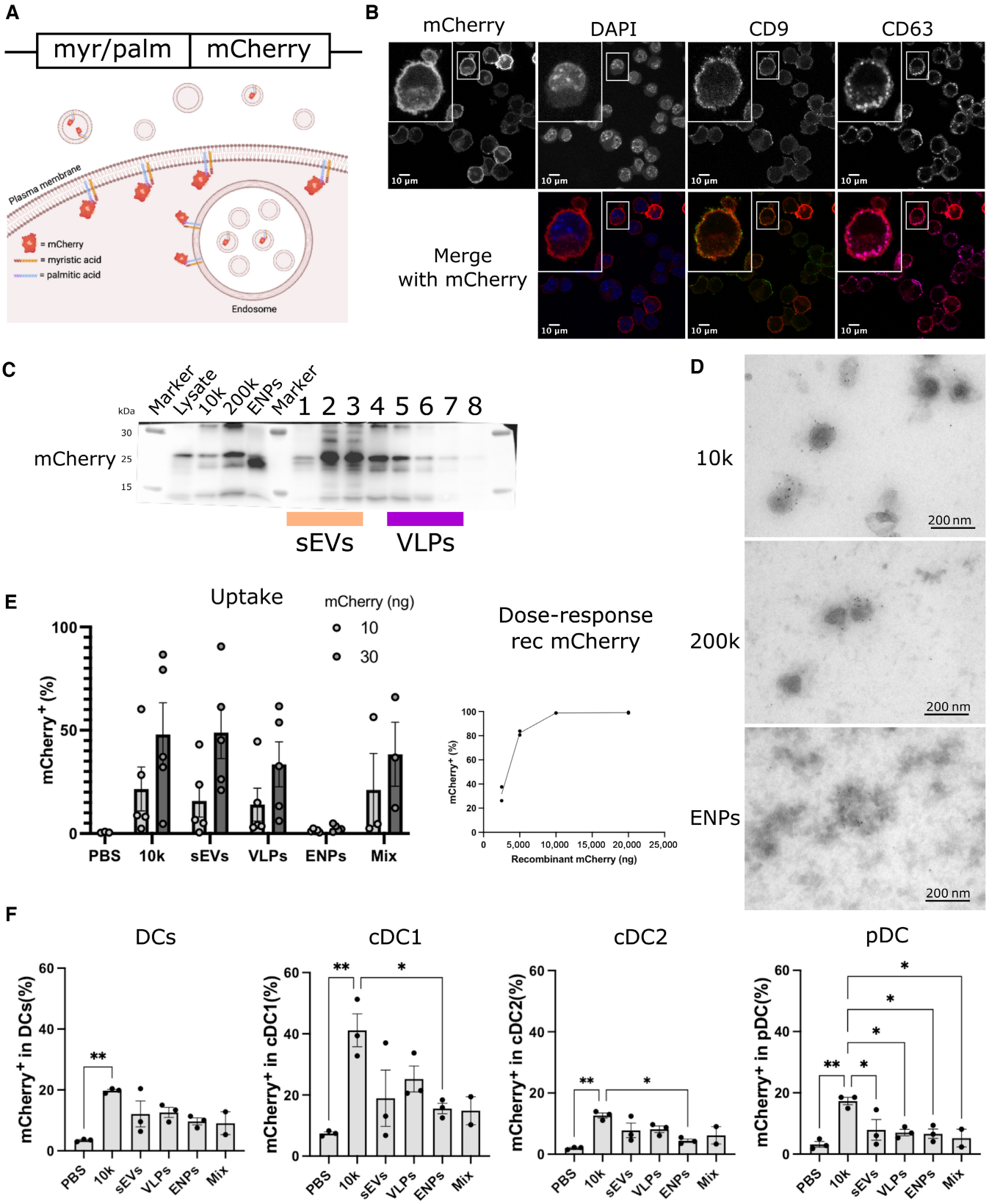
A
myr/palm
mCherry
Plasma membrane
= mCherry
= myristic acid
= palmitic acid
Endosome
B
mCherry
DAPI
CD9
CD63
Merge with mCherry
10 µm
C
Marker
Lysate
10k
200k
ENPs
Marker
1 2 3 4 5 6 7 8
kDa
30
25
15
mCherry
sEVs
VLPs
D
10k
200k
ENPs
200 nm
E
Uptake
mCherry (ng)
10
30
mCherry+ (%)
100
50
0
PBS
10k
sEVs
VLPs
ENPs
Mix
Dose-response rec mCherry
mCherry+ (%)
Recombinant mCherry (ng)
0
5,000
10,000
15,000
20,000
25,000
F
DCs
cDC1
cDC2
pDC
mCherry+ in DCs(%)
mCherry+ in cDC1(%)
mCherry+ in cDC2(%)
mCherry+ in pDC(%)
PBS
10k
sEVs
VLPs
ENPs
Mix

Figure 5.

Figure 5. Protein transfer capacity of the different subtypes of particles.

A Scheme of the construct containing the myristoylation and palmitoylation sequences fused to mCherry, which was used to create the EO771 myr/palm-mCherry stable cells (top) and scheme of expected intracellular and intravesicular distribution of myr/palm-mCherry (bottom, created by Biorender.com).

B Confocal microscopy of EO771-myr/palm-mCherry cells showing DAPI in blue and mCherry in red, CD9 in green and CD63 in magenta (overlay and close-ups).

C Western blot loaded with EVs/ENPs from 20 × 10^6 cells hybridized with anti-mCherry, showing its presence in the different subtypes of particles (same gels as in Figs 1B and 2C and D).

D Immunostaining with anti-mCherry (5 nm gold particles) and transmission electron microscopy (TEM) analysis of saponin permeabilized 10k, 200k and ENPs from EO771 m/p-mCherry.

E Uptake by MutuDC, quantified by flow cytometry (expressed as % of $mCherry^+$ cells), of 10 or 30 ng of mCherry from each subtype of particle (left, $n = 5$), or a dose–response of recombinant mCherry (right, $n = 2$).

F Uptake by spleen DCs of 30 ng of mCherry from each subtype of particle. Results are presented for total $CD11c^+$ DCs, and subtypes of DCs: cDC1, cDC2, and pDCs (defined as in Appendix Fig S1B). One way ANOVA with Tukey's multiple comparison test was performed, $n = 3$. *$P < 0.05$ and **$P < 0.01$. n = number of biological replicates (i.e. independent EV preparations) (E and F). Error bars = SEM (E and F).

Source data are available online for this figure.

subtypes, the 10k was significantly taken up, as compared to the PBS control and to ENPs, whereas the VLPs, sEVs, and Mix showed some level of uptake, but not significantly different from the PBS control. cDC1, the DC subtype specialized in cross-presentation, were the cells displaying the highest uptake capacity, mainly of the 10k, but also (although not significantly) of other EVs and ENPs.

Our results demonstrate that the mixed EV-containing 10k is successfully captured and recognized by DCs, with a better efficiency compared to ENPs or free soluble protein.

The 10k is the scaffold that leads to the highest cross-presentation

Finally, to directly address the capacity of EVs/ENPs to induce presentation of antigens by target DCs, we used OVA as a model antigen, fused to the same myr/palm sequence used with mCherry, to allow its targeting to EVs/ENPs, and to a myc tag for detection (Fig 6A). In EO771 cells stably expressing the resulting protein, OVA was detected as bands of different sizes in the secreted EVs and particles, and most prominently in the 10k (Fig 6B). The amount of OVA was quantified in each sample as compared to known concentrations of recombinant OVA loaded on the same western blot, and rapported to either the number of secreting cells (Fig 6C, left), or to the number of particles (Fig 6C, right). Like for mCherry uptake, OVA concentration was used to normalize the amount of each fraction used for the cross-presentation experiments.

MutuDC cells were exposed to 1 or 2 ng of OVA associated with the different carriers for 5 h, then washed and co-cultured with OT1 cells, expressing a TCR that recognizes specifically the SIINFEKL peptide of OVA presented on MHC-I H2-Kb molecules (Fig 6D). After 18 h, activation of OT1 T cells was measured by flow cytometry, quantifying expression of the activation markers CD69 and CD25 (Fig 6E–G). In this assay, the most efficient (and only statistically significant) activation of T cells was observed in the presence of MutuDC exposed to 10k. MutuDC exposed to VLPs or to Mix induced a very low, but clearly above background (although not significantly different from PBS control), level of OT1 activation, while MutuDC exposed to sEVs and ENPs did not activate at all the T cells. When normalized to the amount of recombinant OVA needed to obtain similar activation levels (Fig 6H), the 10k was the most efficient at presenting antigens to MutuDCs, followed by VLPs and the Mix (Fig 6I).

Discussion

Tumor-derived EVs have been proposed as a source of tumor antigen and as immune regulators in the tumor microenvironment. However, the bibliography is contradictory, attributing to tumor EVs both immuno-activating and immuno-suppressive roles (Thery *et al*, 2009; Robbins & Morelli, 2014; Greening *et al*, 2015). These discrepancies could be explained by differences in the tumor cells used as source of EVs (cell type, cancer stage, culture conditions), but also by the isolation methods, which could result in various mixtures of the EVs and ENPs that a single tumor cell secretes.

In this work, we show that the ENPs and EV subtypes from a mouse mammary adenocarcinoma cell line, EO771, have distinct and even opposite effects on target DCs *in vitro*. Most strikingly, we evidenced a novel, and thus far ignored, subtype of small EVs: VLPs and infectious retroviral particles, which represent a major component of these mouse tumor-derived EV preparations.

The VLPs, defined by the presence of a viral capsid formed by the protein gag, come from endogenous retroviruses (ERVs) with restored infectivity. ERVs are expressed in mice at low levels, but they are non-infectious (Stocking & Kozak, 2008). However, a particular ERV locus of C57BL/6 mice, *Emv2*, encoding for an endogenous ecotropic replication-defective murine leukemia virus (eMLV) carrying a single inactivating mutation in the reverse transcriptase, can by *trans*-complementation of viral proteins and eventually recombination with other endogenous MLV proviruses, become infectious and subsequently expressed at high levels (King *et al*, 1988). In the organism of C57BL/6 mice, the acquisition of infectious potential of this gene is stopped by the immune system in an antibody-dependent manner (Young *et al*, 2012), but in *in vitro*-propagated cell lines, this control process does not take place. The presence of endogenous retroviral proteins (Leong *et al*, 1988; Shepherd *et al*, 2003) and of infectious eMLV (Ottina *et al*, 2018) has been reported in many mouse tumor cell lines. Here, we observed expression of the env and gag MLV proteins in cells and EVs of most mouse tumor cell lines used to study cancer development (Table EV1): 12/14 (of C57Bl/6 and other origins), including carcinoma, melanoma, fibrosarcoma, various hematopoietic cancer cell lines, but not in 2 non-tumoral fibroblasts nor in primary splenocytes. However, VLP presence in EV preparations was not strictly correlated with tumorigenicity of the cells, since we did not detect gag in two lung carcinoma (LLC1 and KP), while we had, 2 decades ago, detected gag in EV isolated from a long-term non-tumoral

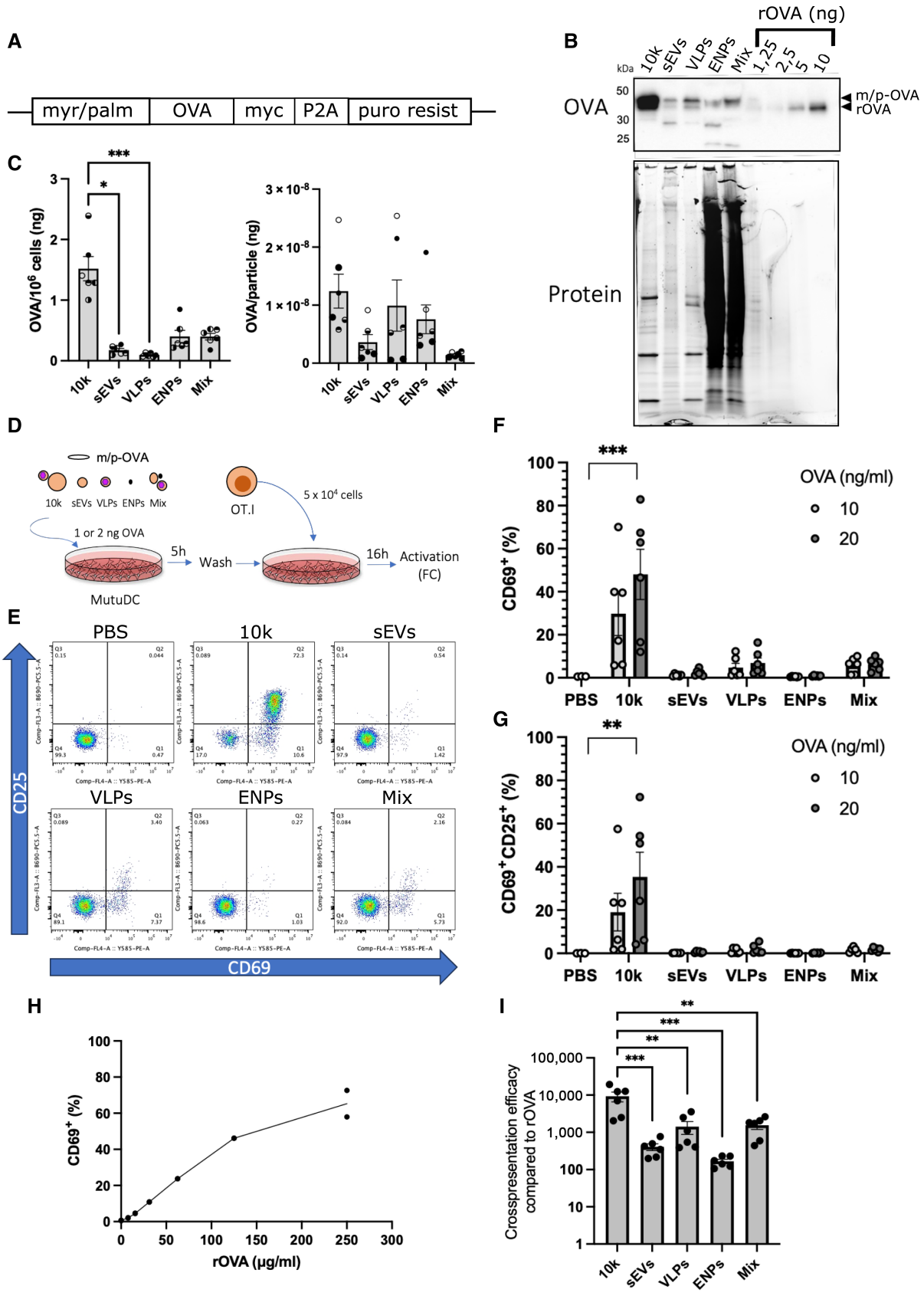
A
myr/palm
OVA
myc
P2A
puro resist
B
rOVA (ng)
10k
sEVs
VLPs
ENPs
Mix
1.25
2.5
5
10
kDa
50
30
25
OVA
m/p-OVA
rOVA
Protein
C
OVA/10^6 cells (ng)
OVA/particle (ng)
D
m/p-OVA
10k sEVs VLPs ENPs Mix
OT.I
5 x 10^4 cells
1 or 2 ng OVA
5h
Wash
16h
Activation (FC)
MutuDC
E
PBS
10k
sEVs
VLPs
ENPs
Mix
CD25
CD69
F
CD69+ (%)
OVA (ng/ml)
10
20
PBS 10k sEVs VLPs ENPs Mix
G
CD69+CD25+ (%)
H
CD69+ (%)
rOVA (µg/ml)
I
Crosspresentation efficacy compared to rOVA

Figure 6.

Figure 6. Cross-presentation of OVA antigen carried by the subtypes of particles.

A Scheme of the construct containing the myristoylation and palmitoylation sequences fused to OVA, myc tag, P2A cleavage site and puromycin resistance gene for selection, which was used to create the EO771 myr/palm-OVA stable cells.

B Analysis of EVs/ENPs from 20 × 10^6 EO771-m/p-OVA by western Blot. Four known amounts of recombinant OVA were loaded on the same gel to allow quantification of OVA. Blots were revealed with a polyclonal antibody against OVA. One representative blot out of 6. Arrowheads indicate the positions of myr/palm-OVA (upper band) and recombinant OVA (lower band).

C Quantification of OVA in the different EVs/ENPs, was done on the western blot images as compared to the OVA dose–response curve. Graphs show ng OVA/10^6 cells (left) or ng OVA/particles (right). Friedman test with Dunn's multiple comparison was performed. $n = 6$.

D Scheme of the protocol of cross-presentation of EV/ENP-OVA cargo by MutuDC to OT1 T cells.

E Dot plots of flow cytometry analysis of OTI cells (CD69 and CD25 expression), 18 h after exposure to MutuDC that had been fed with OVA present in the various types of EVs/ENPs (one representative replicate).

F, G Quantification of $CD69^-$ (F) and double CD69/CD25 (G)- expressing OT1 T cells after exposure to MutuDC that had been fed with OVA present in the various types of EVs/ENPs. Mixed-effects model was performed with Dunnett's multiple comparison to the PBS, the mean of both concentrations was used for the comparisons, with different concentrations as repeated measures, $n = 6$.

H Cross-presentation dose–response using recombinant OVA.

I Cross-presentation efficacy was calculated by dividing the amount of rOVA needed to elicit a certain degree of CD69 expression (fitting the dose–response curve shown in Fig 6H) to the actual amount of OVA present in each EV/ENPs. $n = 6$ (only using the 20 ng/ml condition). Ordinary one-way ANOVA test was performed with Tukey's multiple comparaison. *$P < 0.05$, **$P < 0.01$, and ***$P < 0.001$ (C, F, G, I). Error bars = SEM (C, F, G, I). n = number of biological replicates (i.e. independent EV preparations).

Source data are available online for this figure.

mouse dendritic cell line (Thery *et al*, 1999, 2001). Since endogenous retroviruses are mostly silent in the human genome (Kassiotis & Stoye, 2017), the presence of VLPs may not be as prominent in human tumor-derived cell lines, except those established from retrovirus-induced cancers. However, human endogenous retrovirus (HERV)-derived RNA and DNA have been previously detected in EVs from human gliomas and medulloblastomas (Balaj *et al*, 2011), and there are several reports of retroviral particle production by human placenta and cancer cells (Nelson *et al*, 1978; Keydar *et al*, 1984; Lower *et al*, 1993; Contreras-Galindo *et al*, 2008), thus calling for a more systematic assessment of the presence of VLPs and infectious retroviruses in EVs released by human tumor cell lines.

We explored the effects of the different types of EVs/ENPs on target immune cells by designing a reliable protocol to separate the VLPs and retroviruses from other small EVs and comparing side-by-side their effect on target antigen-presenting cells (DCs). We thus unexpectedly observed that virus-free sEVs induced death of the DCs, whereas VLPs did not display this toxic activity. The mixture of sEVs and VLPs recovered by a classical ultracentrifugation protocol (200k) also displayed some death-inducing activity, although to a lower level than the purified sEVs. Interestingly, this activity was also observed in the 200k pellets from half of the tested cell lines (Table EV1), in a manner that was neither correlated with tumorigenicity, nor with the presence or not of gag or env expression. The molecular determinants of this death-inducing activity are not species-specific, since murine sEVs induced death of human DCs, and they remain to be identified by follow-up studies. The list of proteins specific or strongly enriched in one or the other subtype of EVs, provided by our work (Figs 3 and 4, Dataset EV2), will be a very useful source to explore for candidate proteins responsible for these EV subtype-specific activities. However, other types of molecules, such as nucleic acids or small metabolites, could also be involved in these effects.

Regarding the immunogenicity, our work shows that the 10k containing a large array of different EVs (large, dense, VLPs) is the most immunogenic for DCs, promoting their maturation, cytokine and chemokine secretion, cross-presentation and activation of T cells. DC activation was observed with 10k from most tumor cell lines, whether they expressed or not VLPs, while it was not observed with 10k from the non-tumoral fibroblast Pfa1 (Table EV1). This could suggest that tumor-derived EVs have some immune functions that are tumor-specific, and that DCs are able to differentiate tumor- from non-tumor EVs; however, analysis of additional non-tumoral cell-derived 10k would be required to confirm this hypothesis. Further mechanistic studies will be required to determine the nature of the activation pathways induced by 10k in DCs, although our study provides leads. The quantitative proteomic analysis of DAMPs reveals the most rich and abundant set in the 10k, suggesting that one or several of these proteins are involved in the activation of DCs. This enrichment could be explained by the fact that the 10k includes large EVs that might contain mitochondria or mitochondria-derived vesicles (according to the GO-term enrichment analysis, Fig 3C), or that might be plasma membrane-derived apoptotic bodies (ApoBDs, 500 nm to 2 μm) coming from dying cells in the culture. ApoBDs and mitochondria are rich sources of DAMPs, and ApoBD expose phagocytotic signals and, under stress condition, induce immune activation (Krysko *et al*, 2012; Caruso & Poon, 2018).

On the other hand, when comparing sEVs and VLPs, we observed similar capture by MutuDCs, where both induced some surface expression of maturation markers and low levels of cytokine secretion. However, despite sEVs led to a slightly higher level of cytokine secretion than VLPs, they did not induce cross-presentation of a model antigen they had been engineered to carry (OVA), while VLPs did allow some cross-presentation. Therefore, some of the literature describing immune effects of murine tumor-"exosomes" should be reconsidered, as describing effects of a combination of toxic sEVs (possibly coming from both MVBs and the plasma membrane) and antigen-carrying VLPs and retroviruses. By contrast, the ENPs did not induce any detectable effects on the immune state of the DCs, maturation or cytokine release. This is probably due to their poor efficacy of being captured by MutuDCs, as demonstrated in our uptake assay, as opposed to the capacity of 10k, sEVs and VLPs to be taken up (Fig 5). Therefore, even though other groups have shown that ENPs or supermeres can transfer functional

enzymes or receptors to epithelial cells (Zhang *et al*, 2019, 2021b), this activity does not seem efficient or useful on MutuDCs. Similarly, we and others have shown that the ACE2 enzyme, which is also a receptor for the SARS-CoV2 virus, is present on sEVs, but also as a soluble form (Cocozza *et al*, 2020) or in exomeres (Zhang *et al*, 2021a). However, even though all forms can bind the virus (Zhang *et al*, 2021a), the EV-associated form is much more efficient to decrease viral infectivity (Cocozza *et al*, 2020). Therefore, at least for a purpose of immunogenic stimulation and antigen transfer, or for decoy activities, ENPs, like soluble recombinant proteins, are not the most promising tools.

We postulate that the presence of a lipid bilayer on all EV types makes them good targets for efficient phagocytosis. There is plenty of evidence in the literature that a lipid bilayer promotes recognition and uptake, from classic technics of cells transfection through liposomes (Lasic & Papahadjopoulos, 1995) to specific studies of uptake of nanoparticles (Mosquera *et al*, 2018). In addition, in EVs, the lipid bilayer contains transmembrane receptors and ligands that have counterpart receptors in membranes from target cells, thus facilitating capture. Besides these major factors, some others might be potentiating this effect. For instance, introducing negative charges on soluble OVA antigen was shown to promote its scavenger receptor-dependent uptake by DCs (Shakushiro *et al*, 2004). Interestingly, we observed that all the EV/ENP subtypes were negatively charged, by measure of their zeta potential. However, the ENPs were the least electronegative and most poorly taken up. Another feature of all the highly taken-up EV subtypes is the presence of various envelope proteins of MLV. The env protein can be glycosylated, which makes it recognized by lectin receptors abundantly expressed by both $CD8a^+$ DCs (cDC1) and $CD8^-$ DCs (cDC2). In addition, the lectin receptors could also recognize other glycosylated proteins, abundant on EVs (Williams *et al*, 2018).

In conclusion, it will be interesting to assess whether our findings hold true in purely human settings, as they could then have important consequences for translation of EVs to cancer immunotherapy: a mixed preparation of large and dense EVs, corresponding to the 10k used here, seems a more efficient source of activity than highly purified small EVs or exosomes. However, this should be tested for the different producing cell sources. Conversely, our observation of the cytotoxicity of small EVs, if confirmed for human tumor-derived EVs, opens a new route of immunotherapy, by blocking the immunosuppressive activity of the cytotoxic tumor sEVs.

Materials and Methods

Cells

All cells were kept at 37°C in a humidified atmosphere with 5% CO_2. The medullary breast adenocarcinoma cell line EO771 isolated as spontaneous tumor from a C57BL/6 mouse (Homburger, 1948; Sugiura & Stock, 1952) was purchased from CH3 BioSystems and cultured in RPMI-1640-Glutamax medium (Gibco) supplemented with 10% FBS (Eurobio), 10 mM HEPES (Thermo Fisher Scientific), 50 μM β-mercaptoethanol (Gibco) and 100 U/ml penicillin–streptomycin (Thermo Fisher Scientific). The Balb/c mammary carcinoma 4T1 (originating from ATCC and kindly provided by Dr S. Fiorentino) was cultured as described in Bobrie *et al* (2012) in RPMI-1640-Glutamax medium (Gibco) supplemented with 10% FBS (Eurobio), 10 mM Hepes, 100 U/ml penicillin/streptomycin and 1 mM sodium pyruvate (Thermo Fisher Scientific). The MutuDC cell line established from spleen tumors of CD11c: SV40LgT-eGFP-transgenic C57BL/6 mice was kindly provided by Dr. Hans Acha-Orbea (Fuertes Marraco *et al*, 2012) and cultured in IMDM (Sigma-Aldrich), supplemented with 8% FBS (Biosera), 2 mM Glutamax (Gibco), 10 mM HEPES, 50 μM β-mercaptoethanol and 100 U/ml penicillin–streptomycin. The mouse spontaneously immortalized embryonic fibroblast cell line Pfa1 (Seiler *et al*, 2008) was kindly provided by Dr Sebastian Doll and cultured in DMEM (Thermo Fisher Scientific) supplemented with 10% FBS (Eurobio) and 100 U/ml penicillin–streptomycin. *Mus dunni* and *Mus dunni*-XG7 fibroblasts (CRL-2017) were kindly provided by Dr J.P. Stoye's lab and cultured in IMDM (Sigma-Aldrich), supplemented with 5% FBS (Eurobio), 2 mM Glutamax (Gibco), 50 μM β-mercaptoethanol and 100 U/ml penicillin–streptomycin. Various mouse cell lines available as frozen stocks in our lab were also used: B3Z was cultured in RPMI-1640-Glutamax medium (Gibco) supplemented with 10% FBS (Eurobio) and 100 U/ml penicillin–streptomycin. All other cells (TS/A, B16F10, MCA101, MB49, KP, LLC1, Raw264.7, MC38, EL4 and EG7) were cultured in DMEM (Thermo Fisher Scientific) supplemented with 10% FBS (Eurobio) and 100 U/ml penicillin–streptomycin. All cell lines were checked for mycoplasma contamination each time a batch was frozen and found to be negative.

Mouse female C57BL/6 primary spleen DC were cultured in RPMI-1640-Glutamax medium supplemented with 10% FBS (Biosera), 1% MEM non-essential amino acids (Thermo Fisher Scientific), 1 mM sodium pyruvate, 10 mM HEPES, 50 μM β-mercaptoethanol, and 100 U/ml penicillin–streptomycin.

Human monocyte-derived DCs (MoDCs) were obtained from buffy coats from healthy human donors according to the Helsinki Declaration, with informed consent obtained from the blood donors. Briefly, peripheral blood mononuclear cells (PBMCs) were purified by density gradient centrifugation (LymphoPrep, Axis Shield) as described before (Tkach *et al*, 2017). $CD14^+$ cells were enriched by magnetic sorting (CD14 Microbeads, #130-050-201 Miltenyi Biotec) following manufacturer's instructions. 20–25 million $CD14^+$ cells were cultured in 175 cm^2 flasks in 30 ml of medium RPMI 1640 supplemented with 10% FCS, 10 mM Hepes, 100 IU/ml penicillin and 100 μg/ml streptomycin in the presence of IL-4 and GM-CSF (50 and 100 ng/ml, respectively; Miltenyi Biotec). After 3 days, fresh IL-4 and GM-CSF were added to the culture. Floating monocyte-derived DCs were resuspended and used 5 or 6 days after starting the culture.

Mice

OT1 mice on a $Rag2^{-/-}$ C57BL/6N background (Lantz *et al*, 2000) were bred in the CERFE SPF animal facility (Evry, France) for Institut Curie. At 6–16 weeks age, mice were housed in the Institut Curie animal facility (agreement D75-05-17) for at least 1 week before use. OT1 T cells were obtained by purification with EasySep™ mouse naïve $CD8^+$ T cell isolation kit (Stemcell) from spleen and lymph nodes of OT1 mice, according to the manufacturer's instructions.

PanDCs were isolated from spleen of two female C57BL/6 mice aged 14 weeks, using mouse Pan dendritic cell isolation kit

according to manufacturer's instructions (Miltenyi Biotec) (Vremec & Segura, 2013).

Plasmids and generation of stable EO771 cell lines

The plasmid pmCherry-C1 from Clontech modified to add a myristoylation and palmitoylation sequence plus a linker (ATG**GGCTGCATCAAGAGCAAGCGCAAG**GACAACCTGAACGACGA CGGCGTGG ACgaaccggtcgccacc) in Nterm of mCherry was kindly provided by Dr. Franck Perez (Valenzuela & Perez, 2020; Mathieu *et al*, 2021). myr/palm-mCherry-EO771 cells were sorted based on mCherry expression (S3™ cell sorter, Bio-rad) 3 days after transfection by 5 μl of lipofectamine 2000 (Invitrogen) with 2 μg of the plasmid and regularly re-sorted to maintain expression of myr/palm-mCherry.

For myr/palm-OVA, the pTCP vector (transOMIC) was used as backbone and myristoylation and palmitoylation sequences (same as for mCherry), followed by OVA with in-frame a myc tag, the cleavage peptide P2A and puromycin resistance sequences were included in the coding frame. myr/palm-OVA-EO771 cells were obtained by selection with 4 μg/ml of puromycin, 48 h after transduction with lentivirus from the supernatant (48 h) of HEK293FT transfected with TransIT-293 and 2 μg of the plasmids (pVSVG, pPAX2 and m/p-OVA, proportions 2:5:8). Stable cells were subsequently cultured in the presence of puromycin 2 μg/ml.

EVs and ENPs isolation by differential ultracentrifugation and density gradient

To obtain conditioned medium, EO771, Pfa1, 4T1, TS/A, B16F10, MCA101, MB49, KP, LLC1, Raw264.7, MC38 and *Mus Dunni* murine cells (plated 1–3 days before in complete medium, to reach about 80% confluency) were cultured for 24 h in complete medium without serum (= serum-free medium). MutuDC were cultured for 24 h in complete medium depleted from serum EV. Cell viability was measured at the end of the culture and found to be more than 85%. EV depletion from serum-containing medium was performed by overnight ultracentrifugation at 100,000 *g* in a 45Ti rotor of complete medium containing 20% FCS as described previously (Thery *et al*, 2006). Depleted medium was recovered by pipetting, leaving 1 cm of medium above the pellet, before 0.22 μm filtration for sterilization (Liao *et al*, 2019). Conditioned medium was harvested, and the isolation protocol was performed in sterile conditions at 4°C. The conditioned medium (90–300 ml) from 100 to 600 × 10^6 cells was centrifuged at 350 *g* for 10 min at 4°C. Then (Fig 2F), the supernatant was centrifuged at 2,000 *g* for 20 min at 4°C and the 2k pellet was discarded. The supernatant was concentrated with Millipore filters (MWCO = 10 kDa, 70 ml) down to 6 ml and ultracentrifuged at 10,000 *g* for 16 min at 4°C in MLA-80 rotor (Beckman Coulter). The pellet was resuspended and washed with PBS at the same conditions (volume, speed and time), as well as for all the washes in this protocol. The obtained pellet was resuspended in PBS at 0.2 μl/10^6 cells and called 10k. The supernatant of the first 10,000 *g*, depending on the case, was divided in two: one fraction was ultracentrifuged at 200,000 *g* for 50 min at 4°C in MLA-80 rotor to obtain the 200k followed by a wash in the same volume of PBS and the same centrifugation conditions. The 200k pellet was either resuspended at 1 μl/10^6 cells of PBS or resuspended in 1 ml of PBS to seed on top of the velocity gradient to obtain the sEVs and VLPs; the other fraction was ultracentrifuged at 200,000 *g* in MLA-80 rotor overnight at 4°C in order to obtain the Mix (washed in 6 ml of PBS by overnight centrifugation at 200,000 *g* and resuspended at 1 μl/10^6 cells). The velocity gradient was prepared by adding 5 layers of iodixanol at decreasing concentrations, bottom to top: 22, 18, 14, 10 and 6% and ultracentrifuged at 187,000 *g* for 1 h 30 min at 4°C in Sw32.1Ti rotor (Beckman Coulter). Afterwards, 8 fractions of 2 ml were collected carefully from top to bottom, washed by adding 4 ml of PBS and centrifuging at 200,000 *g* for 50 min at 4°C, and resuspended at 0.5 μl/10^6 cells of PBS. The pellets were kept separated or pooled 1–3 (sEVs) and 5–7 (VLPs). The supernatant of the 200,000 *g* for 50 min was ultracentrifuged at 200,000 *g* in MLA-80 rotor overnight at 4°C and washed to obtain the ENPs (finally resuspended at 1 μl/10^6 cells). Samples were aliquoted and stored at −80°C.

EVs and ENPs separation by asymetric flow Field-Flow fractionation (AF4)

An AF4 long channel with a frit inlet coupled to the eclipse system (Wyatt Technology, Santa Barbara, CA, USA) was driven by an isocratic pump system including a degasser and an autosampler (Shimadzu, Kyoto, Japan). Detection was performed by an ultraviolet (UV) detector at 280 nm (Shimadzu) and a multi-angle light scattering (MALS) Dawn Helios-II using a laser at 658 nm (Wyatt Technology). The channel was set up with a 350 μm spacer and a 10 kDa regenerated cellulose membrane (Wyatt Technology). PBS supplemented with 0.02% w/v NaN_3 (TCI chemicals, Tokyo, Japan) and filtered with 0.1 μm polyethersulfone filter (Sigma-Aldrich, Merck Life Science) was used as a mobile phase. All runs were performed at room temperature (20–25°C).

A detector flow of 1 ml/min was applied in the channel and the sample was injected with an inject flow rate of 0.2 ml/min. An initial cross flow of 2 ml/min for 5 min was applied. Subsequently, the cross flow decreased exponentially from 2 ml/min to 0.1 ml/min over 50 min. The protocol was finished by cleaning the channel from all remaining components using a cross flow of 0 ml/min for 10 min. The elution inject mode was used during the entire run.

The Voyager software (Wyatt Technology) was used for data acquisition and the Astra software version 7.3.2 (Wyatt Technology) was used for data analysis. Baseline subtraction was performed. For size distribution analysis the weight density method with results fitting was applied. The sphere model was used. The refractive index for EVs (1.37) was added for correct number density estimation. Light scatter (in relative signal), diameter (in nm) and UV absorption (280 nm) were plotted against time.

The AF4 eluted fractions were collected during time and pooled as indicated in Fig EV2B and concentrated to 65 μl using Amicon Ultra-2 10K filters (Merck Life Science).

EV characterization

Exhaustive EV subtype characterization was performed according to the MISEV guidelines (Thery *et al*, 2018). All relevant data of the experiments were submitted to the EV-TRACK knowledgebase (EV-TRACK ID: EV230008) (EV-TRACK Consortium *et al*, 2017) https://evtrack.org/search.php.

Western blot

Cell lysates from 2×10^5 cells, EVs and ENPs secreted by 20×10^6 cells were resuspended in Laemmli sample buffer (Bio-Rad), boiled 10 min at 95°C and run in 4–15% Mini-Protean TGX Stain-Free gels (Bio-Rad) in non-reducing conditions (no β-mercaptoethanol nor DTT). Immuno-Blot PVDF membranes (Bio-Rad) were developed using Immobilon forte western HRP substrate (Millipore). The antibodies used were anti-mouse: CD63 1/200 (clone R5G2, MBL, D263-3), CD9 1/1000 (clone KMC8, BD Bioscience, 553758), Alix 1/1000 (clone 3A9, Cell Signaling, 11/2012), MFGE8 1/1000 (clone 18A2-G10, MBL, D199-3), Hsp90 1/1000 (clone AC88, Enzo Lifescience, ADI-SPA-830-F), Argonaute2 1/1000 (Cell Signaling, 2897), MHC I 1/1000 (rabbit-anti-mouse MHCI, made and kindly provided by Dr H. Ploegh, Boston) (Veron *et al*, 2005), 14-3-3 (clone EPR6380, Abcam, ab125032). Anti p30 gag MLV 1/1000 (clone R187), env MLV 1/2000 (clone 83A25) were kindly provided by Dr Leonard Evans. Rabbit anti-OVA 1/1000 was from Rockland (200-401-033) and rabbit anti-mCherry 1/1000 from Biovision (5993).

Nanoparticle tracking analysis (NTA)

Particle concentration, size distribution and zeta potential were measured using ZetaView PMX-120 (Particle Metrix) with software version 8.04.02. Sensitivity was set at 76 and shutter at 70, 11 positions and frame rate at 30. An aliquot of 1 µl from each sample was used for the measurements and dilutions vary between 1/1,000 and 1/100,000 depending on the concentration of the sample.

Cryo-electron microscopy (EM)

Cryo-EM was performed on −80°C frozen samples. Lacey carbon 300 mesh grids (Ted Pella, USA) were used in all cryo-EM experiments. Blotting was carried out on the opposite side from the liquid drop and samples were plunge frozen in liquid ethane (EMGP, Leica, Germany). Cryo-EM images were acquired with a Tecnai G2 (Thermo Fisher Scientific, USA) Lab6 microscope operated at 200 kV and equipped with a 4k × 4k CMOS camera (F416, TVIPS). Image acquisition was performed under low dose conditions of 10 $e^-/Å^2$ at a magnification of 50,000 or 6,500 with a pixel size of 0.21 or 1.6 nm, respectively.

Immuno-transmission EM

Electron microscopy was performed on EV and ENP pellets from myr/palm-mCherry and myr/palm-OVA EO771 cells as control, resuspended in PBS and stored at −80°C that had never been thawed and re-frozen. Staining with anti-mCherry antibody was performed according to the Protein A-gold method (Slot & Geuze, 2007), on EVs adsorbed for 20 min to formvar/carbon–coated copper/palladium grids followed by fixation in 2% paraformaldehyde for 20 min, saturation in PBS-glycine (5 × 1 min), permeabilization in PBS-BSA 1%-Saponin 0.1% or 15 min (Sigma). Immunostaining was performed by incubating with rabbit anti-mCherry (Genetex GTX128508, 1/50) for 1 h, 4 × 2 min washes in PBS, followed by incubation with 5 nm protein-A-gold (CMC, Utrecht, The Netherlands, 1/50) for 20 min, 3 × 5 s + 4 × 2 min washes in PBS, and fixation for 5 min with 1% glutaraldehyde w/v in PBS (Electron Microscopy Sciences). Subsequently, after a wash on 10 droplets of distilled water, grids were transferred to droplets of 0.4% (w/v) uranyl acetate (UA) staining and 1.8% (w/v) methylcellulose embedding solution. After 10 min of incubation, grids were picked up in a wire loop. Most of the excess of the viscous embedding solution was drained away with filter paper after which the grids with sections were air-dried forming a thin layer of embedding solution. Images were acquired with a digital camera Quemesa (EMSIS GmbH, Münster, Germany) mounted on a Tecnai Spirit transmission electron microscope (FEI Company) operated at 80 kV.

Protein quantification

Micro BCA™ Protein Assay kit (Thermo Scientific) was used for the protein quantification. An aliquot of 1–5 µl from each sample was used for the measurements and diluted in a final volume of 150 µl.

Murine leukemia virus infectivity assay

The infectivity capacity of the MLV-containing samples was assessed as previously described (Young *et al*, 2012). Briefly, the 200k obtained from 10×10^6 EO771 or MutuDC cells was added in the presence of polybrene (10 µg/ml) to 3×10^5 *Mus dunni* cells transduced with the replication defective plasmid XG7 encoding for GFP (*Mus dunni-XG7*) in a 6-well plate. The cells were maintained for 14 days in culture, passaged every 2–3 days diluted 1/10–1/25, and production of the XG7 pseudotyped virus was evaluated by incubation of their supernatant with untransduced *Mus dunni* cells. Briefly, 3×10^3 *Mus dunni* cells were incubated with 100 µl of supernatant in the presence of polybrene, and GFP expression was measured by flow cytometry after 3 days.

The above assay is qualitative but not quantitative. Thus, we also quantified efficacy of transfer of viral env protein to target cells by flow cytometry. *Mus Dunni* cells were exposed to 0–40 µg/ml of the different EV subtypes in 100 µl of EV-depleted medium for 24 h. Cells were then washed with PBS, trypsinized for 3 min and labeled with anti-env (83A25, 1/200) followed by anti-mouse-AF647 1/1000. Env exposure on cells was analyzed by flow cytometry.

Qualitative and quantitative proteomic analyses

For the qualitative analysis (Fig EV1B, Dataset EV1), 200k pellets from EO771 or 4T1 and 200k + 10k pellets of MutuDC (10 µg, one biological replicate each) were used. For the quantitative analysis (Fig 3, Dataset EV2), 5 biological replicates of the 10k, sEVs, VLPs, ENPs and Mix (20 µg each) were used.

Sample preparation

Samples were resuspended in 5 µl (qualitative) or 10 µl (quantitative) (2 µg/µl) of 8 M urea, 200 mM ammonium bicarbonate, respectively. After reduction with 5 mM DTT for 30 min at 57°C and alkylation with 10 mM iodoacetamide for 30 min at room temperature in the dark, samples were diluted in 100 mM ammonium bicarbonate to reach a final concentration of 1 M urea. For the qualitative analysis, the 200k pellets were digested for 2 h at 37°C with 0.4 µg of Trypsin/Lys-C (Promega CAT#: V5071) and then overnight by adding 0.4 µg of Trypsin/Lys-C. For quantitative analyses, samples were digested overnight at 37°C with Trypsin/Lys-C at a ratio of 1/50. Digested samples were loaded onto homemade C18 StageTips for desalting, then eluted using 40/60 MeCN/H_2O + 0.1% formic acid and vacuum concentrated to dryness. Peptides were reconstituted in 10 µl of injection buffer in 0.3% trifluoroacetic acid (TFA) before liquid chromatography–tandem mass spectrometry (LC–MS/MS) analysis.

LC–MS/MS analysis

Peptides for the qualitative analysis were separated by reversed phase LC on an RSLCnano system (Ultimate 3000, Thermo Fisher Scientific) coupled online to an Orbitrap Fusion Tribrid mass spectrometer (Thermo Fisher Scientific). Peptides were trapped in a C18 column (75 µm inner diameter × 2 cm; nanoViper Acclaim PepMap 100, Thermo Fisher Scientific) with buffer A (2/98 MeCN:H_2O in 0.1% formic acid) at a flow rate of 3.0 µl/min over 4 min to desalt and concentrate the samples. Separation was performed using a 40 cm × 75 µm C18 column (Reprosil C18, 1.9 µm, 120 Å, Pepsep PN: PSC-40-75-1.9-UHP-nC), regulated to a temperature of 40°C with a linear gradient of 3–32% buffer B (100% MeCN in 0.1% formic acid) at a flow rate of 150 nl/min over 91 min. Full-scan MS was acquired using an Orbitrap Analyzer with the resolution set to 120,000, and ions from each full scan were higher-energy C-trap dissociation (HCD) fragmented and analyzed in the linear ion trap.

For the quantitative analyses, liquid chromatography (LC) was performed as above with an RSLCnano system (Ultimate 3000, Thermo Scientific) coupled online to an Orbitrap Eclipse mass spectrometer (Thermo Fisher Scientific). Peptides were trapped onto the C18 column at a flow rate of 3.0 µl/min in buffer A for 4 min. Separation was performed on a 50 cm nanoviper column (i.d. 75 µm, C18, Acclaim PepMapTM RSLC, 2 µm, 100 Å, Thermo Scientific) regulated to a temperature of 50°C with a linear gradient from 2 to 25% buffer B at a flow rate of 300 nl/min over 91 min. MS1 data were collected in the Orbitrap (120,000 resolution; maximum injection time 60 ms; AGC 4×10^5). Charges states between 2 and 7 were required for MS2 analysis, and a 60 s dynamic exclusion window was used. MS2 scan were performed in the ion trap in rapid mode with HCD fragmentation (isolation window 1.2 Da; NCE 30%; maximum injection time 35 ms; AGC 10^4).

Mass spectrometry data analysis

For identification, the data were searched against the *Mus musculus* (UP000000589_10090) UniProt database and a manually curated list of murine virus protein sequences using Sequest-HT through Proteome Discoverer (version 2.4). The database of murine virus proteins includes protein sequences from all known mouse endogenous and exogenous retroviruses (523 sequences manually extracted from Swissprot) and from endogenous MLV envelope glycoproteins (53 sequences), translated from the nucleotide sequences of proviruses annotated as previously described (Attig *et al*, 2017). Enzyme specificity was set to trypsin and a maximum of two-missed cleavage sites were allowed. Oxidized methionine, Met-loss, Met-loss-Acetyl and N-terminal acetylation were set as variable modifications. Carbamidomethylation of cysteins was set as fixed modification. Maximum allowed mass deviation was set to 10 ppm for monoisotopic precursor ions and 0.6 Da for MS/MS peaks. The resulting files were further processed using myProMS (Poullet *et al*, 2007) v3.9 (https://github.com/bioinfo-pf-curie/myproms). FDR calculation used Percolator (The *et al*, 2016) and was set to 1% at the peptide level for the whole study. Proteins were considered expressed if identified with at least three peptides among five replicates. The label free quantification was performed by peptide Extracted Ion Chromatograms (XICs), reextracted across all conditions and computed with MassChroQ version 2.2.1 (Valot *et al*, 2011). For protein quantification, XICs from proteotypic and non-proteotypic peptides were used by assigning to the best protein, peptides shared by multiple match groups, and missed cleavages, charge states and sources were allowed. Median and scale normalization was applied on the total signal to correct the XICs for each biological replicate ($N = 5$) for total signal and global variance biases. Label-free quantification (LFQ) was performed following the algorithm as described (Cox *et al*, 2014) with the minimum number of peptide ratios set to 2 and the large ratios stabilization feature. The final LFQ intensities were used as protein abundance.

For principal component analysis (PCA), data were filtered to only allow proteins with at least 3 quantified peptide ions per sample, and with all missing values allowed across all samples. The LFQ values of the 3,200 proteins selected were log10-transformed, and the remaining (27%) missing values were imputed using the R package missMDA (Josse & Husson, 2016).

State-specific protein analysis (SSPA) is an in-house statistical assay that provides statistical ground to the potential state-specificity of a protein (typically: present vs. absent) based on the distribution of its missing values. To perform this test, peptides XICs are summed for each protein and the resulting value is converted into pseudo-counts by $\log_2$-transformation and background subtraction so that the lowest pseudo counts are no smaller than 1. Missing values are converted into 0. For each protein, compared states are then ordered by decreasing mean of their replicates (computed after outlier exclusion) and split into 2 sets (of states) at the largest difference between means of 2 consecutive states (largest step). The protein is declared as overexpressed in the first set and underexpressed in the second. The extent of overexpression is represented by the "best delta" which is the ratio of the largest step over the biggest mean. A statistical test relying on the general linear model with a negative binomial law is also performed to estimate the significance of the difference of means between the 2 sets. Finally, the *P*-values obtained for the whole dataset are corrected for multiple testing according to the Benjamini-Hochberg (FDR) method.

For heatmap representations, log10-transformed LFQ values for proteins with more than three peptides were used. Euclidean distances were calculated for the clustering of proteins (rows) and samples (columns). Pheatmap R package was used for representation. All proteins were used for Fig EV4A. The top 15 or 10 most significantly enriched proteins of each sample type (proteins with delta ≥50 ranked by adjusted *P*-value according to SSPA) were selected for representation in Fig 3D. The 46 quantified viral proteins were used for Fig 3E. Proteins described as DAMPs or PAMPs in (Hoshino *et al*, 2020) were selected for representation in Fig 4I.

GO-enrichment for Cellular Component was used in two analyses: (i) the top 100 most expressed proteins and (ii) the top 100 most SSPA-specific proteins in each group of particles. Enrichr R package was used for enrichment calculations (Kuleshov *et al*, 2016), and ggplot2 was used for representation.

mCherry and OVA quantification

The amount of mCherry present in each sample was quantified measuring the fluorescence (excitation 585/emission 625) of 50 µl of each sample through a spectrophotometer (SpectraMax iD3), side-by-side with a standard curve of recombinant mCherry of known concentration.

The amount of OVA in each sample was calculated from the signal intensity of the ~40 kDa band, in the western blot revealed with anti-OVA antibody, using the curve of recombinant OVA

with known concentration. Intensity of the bands was quantified using Image Lab software (Bio-rad).

Uptake, viability and activation assay

MutuDC, isolated murine panDC or human MoDCs were seeded at 1×10^5 in round bottom 96 well-plates in 50 µl of complete IMDM depleted from serum-derived EVs by overnight ultracentrifugation at 100,000 *g*. Then, 1 or 2 µg of protein or 0.5 to 4×10^9 particles corresponding to 0.2 to 200 µg of proteins, or mixtures of 4×10^9 total particles of sEVs and VLPs in ratios ranging from 1/0 to 1/7 (for the phenotypic change assays), or 10 or 30 ng of mCherry (for the uptake assays) of the EVs and ENPs from EO771 m/p-mCherry or controls (medium alone, recombinant mCherry, LPS-EB ultrapure 10 µg/ml (Invivogen) and CpG 2 µg/ml (TriLink)) were added in a final volume of 100 µl. After 16 h at 37°C, cells were harvested and the supernatant was frozen for later quantification of released cytokines. For MutuDC, cells were stained with Fixable viability dye eFluor™ 780, FcR blocked and stained with fluorochrome-coupled antibodies against mouse: CD40-PerCP-eFluor710, 1/200 (46-0401-80, ThermoFisher), CD86-PE-Cy7, 1/400 (560582, BD Biosciences), PDL1-APC, 1/400 (564715, BD Biosciences) and MHC-II-eFluor 450, 1/200 (48-5320-82, ThermoFisher) or their respective isotypes controls. For panDC, cells were FcR blocked and stained with: B220-FITC, 1/200 (553087, BD Biosciences), CD11c-PerCP-Cy5.5, 1/200 (117328, BioLegend), CD86-PE-Cy7 1/400 (560582, BD Biosciences), XCR1-AF647, 1/200 (148214, BioLegend), MHC-II-APC-Cy7, 1/200 (107628, BioLegend), CD40-BV605, 1/200 (745218, BD Biosciences) and CD172a-BUV737, 1/200 (741819, BD Biosciences) or their respective isotypes controls. Cells were then stained with DAPI (0.1 µg/ml, D3571, ThermoFisher). For human DCs, cells were stained with LIVE/DEAD™ fixable aqua dead cell stain (L34957, ThermoFisher) and fluorochrome-coupled antibodies against human: CD11c-PC7 1/250 (337216, Biolegend), CD1a-PE 1/1000 (300106, Biolegend), BDCA1-PerCP eFluor710 1/50 (46-0015-42, eBioscciences). Cells were analyzed with a Cytoflex cytometer (Beckman). PMTs were first set following recommendation of the cytometer, and adjusted if needed to obtain signal at 0 for unstained samples and not saturated in the positive controls. Compensation was performed with single-stained UltraComp eBeads (Thermo Fisher). Data were analyzed with FlowJo software. For each assay, results are represented as individual biological replicates, each corresponding to a different set of EV/ENP preparation and/or a different source of target cells (different donors of monocytes or spleen cells). Sample size ranges from 2 to 10 replicates. No samples were excluded. Results were analyzed in a non-blinded manner.

Cytokine bead array

A customized set of 17 murine cytokines (IFNγ, IL2, IL5, IL4, IL6, MCP1 (CCL2), IL13, IL10, IL17a, MIP1α, TNFa, MIP1β, IL12 p70, RANTES (CCL5), MIG (CXCL9), IL1α, IL1β), most reported to be secreted by DCs (Morelli *et al*, 2001) was selected to measure in the supernatant of the MutuDC by Cytometric Bead Array (BD CBA Flex Sets) following the manufacturer's recommendations. 15 µl of each culture supernatant was used for the assay. Samples were acquired on a BD FACS verse cytometer and analyzed with the FCAP Array software.

Cross-presentation assay

MutuDC were seeded at 1×10^4 cells in round bottom 96 well-plates with complete EV-depleted RPMI and incubated for 5 h with 1 or 2 ng of OVA in the EVs and ENPs or controls (medium alone, recombinant OVA and SIINFEKL peptide curves). After that, they were washed once with 37°C RPMI and cocultured with 5×10^4 OT1 T cells obtained by purification with EasySep™ mouse naïve $CD8^+$ T cell isolation kit (Stemcell) from spleen and lymph nodes of OT1-Rag mice. After 16 h, cells were harvested and activation of the OT1 was measured by CD69 (553237, BD Pharmingen) and CD25 (551071, BD Biosciences) expression. Cells were also stained with Vα2 TCR (560624, BD Pharmingen) and CD8a (553035, BD Pharmingen) for identification. Cells were analyzed with a Cytoflex cytometer (Beckman). Data were analyzed with FlowJo software.

Data availability

EO771-myr/palm-mCherry and EO771-myr/palm-OVA are available upon request to the corresponding author. The mass spectrometry proteomics raw data are deposited to the ProteomeXchange Consortium via the PRIDE partner repository (Perez-Riverol *et al*, 2022) with the dataset identifier number PXD039715 (http://www.ebi.ac.uk/pride/archive/projects/PXD039715).

Expanded View for this article is available online.

Acknowledgements

We thank Drs J. Helft, L. Saveanu, H. Acha-Orbea, L. Evans, J.P. Stoye, G. Boncompain, S. Doll, S. Fiorentino, L. Alaoui, M. Burbage, M. Gros, M. Rehmsmeier, L. Ringrose, and C. Basse for fruitful discussions and tools. This work was funded by INSERM, CNRS, Institut Curie (including NCI.NIH.PIC3i.2018), French IdEx and LabEx (ANR-10-IDEX-0001-02 PSL), the MSCA-ITN grant "TRAIN-EV" agreement No 722148, grants from Fondation Chercher et Trouver, french ANR (ANR-18-CE13-0017-03; ANR-18-CE15-0008-01; ANR-18-CE16-0022-02), INCa (INCa_11548, INCa_16083), Fondation ARC (PGA1 RF20180206962 and PGA120210200003189_3588), FRM (FDT202106013265, EQU201903007925 and DGE20121125630), Cancéropôle Île-de-France (2013-2-EML-02-ICR-1), financial support from "la Région Île-de-France" (N°EX061034) and ITMO Cancer of Aviesan and INCa on funds administered by Inserm (N°21CQ016-00) for MS analysis. This work was supported by the Francis Crick Institute (CC2088), which receives its core funding from Cancer Research UK, the UK Medical Research Council, and the Wellcome Trust. We also acknowledge the following Core facilities of Institut Curie: Cell and Tissue Imaging (PICT-IBiSA), member of the French national research infrastructure France-BioImaging (ANR10-INBS-04) for fluorescence and electron microscopy, cytometry for assistance in data acquisition, Extracellular Vesicles for assistance in EV isolation and NTA-based quantification.

Author contributions

Federico Cocozza: Conceptualization; data curation; formal analysis; investigation; visualization; methodology; writing – original draft; writing – review and editing. **Lorena Martin-Jaular:** Conceptualization; formal analysis; validation; investigation; methodology; writing – review and editing. **Lien Lippens:** Formal analysis; investigation; methodology.

Aurelie Di Cicco: Investigation; visualization; methodology. **Yago A Arribas:** Data curation; software; formal analysis; writing – review and editing. **Nicolas Ansart:** Investigation; methodology. **Florent Dingli:** Data curation; investigation; methodology. **Michael Richard:** Data curation; software. **Louise Merle:** Investigation; methodology; writing – review and editing. **Mabel Jouve San Roman:** Investigation; methodology. **Patrick Poullet:** Data curation; software; writing – review and editing. **Damarys Loew:** Data curation; formal analysis; writing – review and editing. **Daniel Lévy:** Formal analysis; visualization; methodology; writing – review and editing. **An Hendrix:** Formal analysis; methodology; writing – review and editing. **George Kassiotis:** Resources; formal analysis; funding acquisition; methodology; writing – review and editing. **Alain Joliot:** Formal analysis; investigation; methodology; writing – review and editing. **Mercedes Tkach:** Conceptualization; data curation; formal analysis; supervision; investigation; methodology; writing – original draft; writing – review and editing. **Clotilde Théry:** Conceptualization; formal analysis; supervision; funding acquisition; investigation; writing – original draft; project administration; writing – review and editing.

Disclosure and competing interests statement

GK is co-founder of EnaraBio and a member of its scientific advisory board. MT is currently an employee of Egle Therapeutics. Both companies are involved in search of anti-cancer therapies. CT and MT are inventors of a patent on immuno-therapeutic use of EVs. The other authors have no interests to disclose.

References

Attig J, Young GR, Stoye JP, Kassiotis G (2017) Physiological and pathological transcriptional activation of endogenous retroelements assessed by RNA-sequencing of B lymphocytes. *Front Microbiol* 8: 2489

Balaj L, Lessard R, Dai L, Cho YJ, Pomeroy SL, Breakefield XO, Skog J (2011) Tumour microvesicles contain retrotransposon elements and amplified oncogene sequences. *Nat Commun* 2: 180

Balint S, Muller S, Fischer R, Kessler BM, Harkiolaki M, Valitutti S, Dustin ML (2020) Supramolecular attack particles are autonomous killing entities released from cytotoxic T cells. *Science* 368: 897 – 901

Banchereau J, Steinman RM (1998) Dendritic cells and the control of immunity. *Nature* 392: 245 – 252

Beck R, Verrax J, Gonze T, Zappone M, Pedrosa RC, Taper H, Feron O, Calderon PB (2009) Hsp90 cleavage by an oxidative stress leads to its client proteins degradation and cancer cell death. *Biochem Pharmacol* 77: 375 – 383

Bobrie A, Krumeich S, Reyal F, Recchi C, Moita LF, Seabra MC, Ostrowski M, Thery C (2012) Rab27a supports exosome-dependent and -independent mechanisms that modify the tumor microenvironment and can promote tumor progression. *Cancer Res* 72: 4920 – 4930

Booth AM, Fang Y, Fallon JK, Yang JM, Hildreth JE, Gould SJ (2006) Exosomes and HIV Gag bud from endosome-like domains of the T cell plasma membrane. *J Cell Biol* 172: 923 – 935

Cantin R, Diou J, Belanger D, Tremblay AM, Gilbert C (2008) Discrimination between exosomes and HIV-1: purification of both vesicles from cell-free supernatants. *J Immunol Methods* 338: 21 – 30

Caruso S, Poon IKH (2018) Apoptotic cell-derived extracellular vesicles: more than just debris. *Front Immunol* 9: 1486

Chulpanova DS, Kitaeva KV, James V, Rizvanov AA, Solovyeva VV (2018) Therapeutic prospects of extracellular vesicles in cancer treatment. *Front Immunol* 9: 1534

Cocozza F, Nevo N, Piovesana E, Lahaye X, Buchrieser J, Schwartz O, Manel N, Tkach M, Thery C, Martin-Jaular L (2020) Extracellular vesicles containing ACE2 efficiently prevent infection by SARS-CoV-2 Spike protein-containing virus. *J Extracell Vesicles* 10: e12050

Contreras-Galindo R, Kaplan MH, Leissner P, Verjat T, Ferlenghi I, Bagnoli F, Giusti F, Dosik MH, Hayes DF, Gitlin SD *et al* (2008) Human endogenous retrovirus K (HML-2) elements in the plasma of people with lymphoma and breast cancer. *J Virol* 82: 9329 – 9336

Cox J, Hein MY, Luber CA, Paron I, Nagaraj N, Mann M (2014) Accurate proteome-wide label-free quantification by delayed normalization and maximal peptide ratio extraction, termed MaxLFQ. *Mol Cell Proteomics* 13: 2513 – 2526

EV-TRACK Consortium; Van Deun J, Mestdagh P, Agostinis P, Akay O, Anand S, Anckaert J, Martinez ZA, Baetens T, Beghein E *et al* (2017) EV-TRACK: transparent reporting and centralizing knowledge in extracellular vesicle research. *Nat Methods* 14: 228 – 232

Fuertes Marraco SA, Grosjean F, Duval A, Rosa M, Lavanchy C, Ashok D, Haller S, Otten LA, Steiner QG, Descombes P *et al* (2012) Novel murine dendritic cell lines: a powerful auxiliary tool for dendritic cell research. *Front Immunol* 3: 331

Gajewski TF, Schreiber H, Fu YX (2013) Innate and adaptive immune cells in the tumor microenvironment. *Nat Immunol* 14: 1014 – 1022

Gould SJ, Booth AM, Hildreth JE (2003) The Trojan exosome hypothesis. *Proc Natl Acad Sci USA* 100: 10592 – 10597

Greening DW, Gopal SK, Xu R, Simpson RJ, Chen W (2015) Exosomes and their roles in immune regulation and cancer. *Semin Cell Dev Biol* 40: 72 – 81

Han L, Lam EW, Sun Y (2019) Extracellular vesicles in the tumor microenvironment: old stories, but new tales. *Mol Cancer* 18: 59

Homburger F (1948) Studies on hypoproteinemia: III. Lymphoid hyperplasia and redistribution of nitrogen caused in mice by transplanted tumors (sarcoma 180 and breast adenocarcinoma EO 771). *Science* 107: 648 – 649

Hoshino A, Kim HS, Bojmar L, Gyan KE, Cioffi M, Hernandez J, Zambirinis CP, Rodrigues G, Molina H, Heissel S *et al* (2020) Extracellular vesicle and particle biomarkers define multiple human cancers. *Cell* 182: 1044 – 1061

Jeppesen DK, Fenix AM, Franklin JL, Higginbotham JN, Zhang Q, Zimmerman LJ, Liebler DC, Ping J, Liu Q, Evans R *et al* (2019) Reassessment of exosome composition. *Cell* 177: 428 – 445

Josse J, Husson F (2016) missMDA: a package for handling missing values in multivariate data analysis. *J Stat Softw* 70: 1 – 31

Kassiotis G, Stoye JP (2017) Making a virtue of necessity: the pleiotropic role of human endogenous retroviruses in cancer. *Philos Trans R Soc Lond B Biol Sci* 372: 20160277

Keydar I, Ohno T, Nayak R, Sweet R, Simoni F, Weiss F, Karby S, Mesa-Tejada R, Spiegelman S (1984) Properties of retrovirus-like particles produced by a human breast carcinoma cell line: immunological relationship with mouse mammary tumor virus proteins. *Proc Natl Acad Sci USA* 81: 4188 – 4192

King SR, Berson BJ, Risser R (1988) Mechanism of interaction between endogenous ecotropic murine leukemia viruses in (BALB/c X C57BL/6) hybrid cells. *Virology* 162: 1 – 11

Krysko DV, Garg AD, Kaczmarek A, Krysko O, Agostinis P, Vandenabeele P (2012) Immunogenic cell death and DAMPs in cancer therapy. *Nat Rev Cancer* 12: 860 – 875

Kuleshov MV, Jones MR, Rouillard AD, Fernandez NF, Duan Q, Wang Z, Koplev S, Jenkins SL, Jagodnik KM, Lachmann A *et al* (2016) Enrichr: a comprehensive gene set enrichment analysis web server 2016 update. *Nucleic Acids Res* 44: W90 – W97

Lantz O, Grandjean I, Matzinger P, Di Santo JP (2000) Gamma chain required for naive $CD4^+$ T cell survival but not for antigen proliferation. *Nat Immunol* 1: 54 – 58

Lasic DD, Papahadjopoulos D (1995) Liposomes revisited. *Science* 267: 1275 – 1276

Leong SP, Muller J, Yetter RA, Gorelik E, Takami T, Hearing VJ (1988) Expression and modulation of a retrovirus-associated antigen by murine melanoma cells. *Cancer Res* 48: 4954 – 4958

Liao Z, Jaular LM, Soueidi E, Jouve M, Muth DC, Schoyen TH, Seale T, Haughey NJ, Ostrowski M, Thery C *et al* (2019) Acetylcholinesterase is not a generic marker of extracellular vesicles. *J Extracell Vesicles* 8: 1628592

Lower R, Boller K, Hasenmaier B, Korbmacher C, Muller-Lantzsch N, Lower J, Kurth R (1993) Identification of human endogenous retroviruses with complex mRNA expression and particle formation. *Proc Natl Acad Sci USA* 90: 4480 – 4484

Martin-Jaular L, Nevo N, Schessner JP, Tkach M, Jouve M, Dingli F, Loew D, Witwer KW, Ostrowski M, Borner GHH *et al* (2021) Unbiased proteomic profiling of host cell extracellular vesicle composition and dynamics upon HIV-1 infection. *EMBO J* 40: e105492

Mathieu M, Nevo N, Jouve M, Valenzuela JI, Maurin M, Verweij FJ, Palmulli R, Lankar D, Dingli F, Loew D *et al* (2021) Specificities of exosome versus small ectosome secretion revealed by live intracellular tracking of CD63 and CD9. *Nat Commun* 12: 4389

McCabe JB, Berthiaume LG (1999) Functional roles for fatty acylated amino-terminal domains in subcellular localization. *Mol Biol Cell* 10: 3771 – 3786

McCabe JB, Berthiaume LG (2001) N-terminal protein acylation confers localization to cholesterol, sphingolipid-enriched membranes but not to lipid rafts/caveolae. *Mol Biol Cell* 12: 3601 – 3617

Morelli AE, Zahorchak AF, Larregina AT, Colvin BL, Logar AJ, Takayama T, Falo LD, Thomson AW (2001) Cytokine production by mouse myeloid dendritic cells in relation to differentiation and terminal maturation induced by lipopolysaccharide or CD40 ligation. *Blood* 98: 1512 – 1523

Morelli AE, Larregina AT, Shufesky WJ, Sullivan ML, Stolz DB, Papworth GD, Zahorchak AF, Logar AJ, Wang Z, Watkins SC *et al* (2004) Endocytosis, intracellular sorting, and processing of exosomes by dendritic cells. *Blood* 104: 3257 – 3266

Mosquera J, Garcia I, Liz-Marzan LM (2018) Cellular uptake of nanoparticles versus small molecules: a matter of size. *Acc Chem Res* 51: 2305 – 2313

Nelson J, Leong JA, Levy JA (1978) Normal human placentas contain RNA-directed DNA polymerase activity like that in viruses. *Proc Natl Acad Sci USA* 75: 6263 – 6267

Nolte-'t Hoen E, Cremer T, Gallo RC, Margolis LB (2016) Extracellular vesicles and viruses: are they close relatives? *Proc Natl Acad Sci USA* 113: 9155 – 9161

Ottina E, Levy P, Eksmond U, Merkenschlager J, Young GR, Roels J, Stoye JP, Tuting T, Calado DP, Kassiotis G (2018) Restoration of endogenous retrovirus infectivity impacts mouse cancer models. *Cancer Immunol Res* 6: 1292 – 1300

Perez-Riverol Y, Bai J, Bandla C, Garcia-Seisdedos D, Hewapathirana S, Kamatchinathan S, Kundu DJ, Prakash A, Frericks-Zipper A, Eisenacher M *et al* (2022) The PRIDE database resources in 2022: a hub for mass spectrometry-based proteomics evidences. *Nucleic Acids Res* 50: D543 – D552

Poullet P, Carpentier S, Barillot E (2007) myProMS, a web server for management and validation of mass spectrometry-based proteomic data. *Proteomics* 7: 2553 – 2556

Qu K, Glass B, Dolezal M, Schur FKM, Murciano B, Rein A, Rumlova M, Ruml T, Krausslich HG, Briggs JAG (2018) Structure and architecture of immature and mature murine leukemia virus capsids. *Proc Natl Acad Sci USA* 115: E11751 – E11760

Robbins PD, Morelli AE (2014) Regulation of immune responses by extracellular vesicles. *Nat Rev Immunol* 14: 195 – 208

Seiler A, Schneider M, Forster H, Roth S, Wirth EK, Culmsee C, Plesnila N, Kremmer E, Radmark O, Wurst W *et al* (2008) Glutathione peroxidase 4 senses and translates oxidative stress into 12/15-lipoxygenase dependent- and AIF-mediated cell death. *Cell Metab* 8: 237 – 248

Shakushiro K, Yamasaki Y, Nishikawa M, Takakura Y (2004) Efficient scavenger receptor-mediated uptake and cross-presentation of negatively charged soluble antigens by dendritic cells. *Immunology* 112: 211 – 218

Shepherd AJ, Wilson NJ, Smith KT (2003) Characterisation of endogenous retrovirus in rodent cell lines used for production of biologicals. *Biologicals* 31: 251 – 260

Slot JW, Geuze HJ (2007) Cryosectioning and immunolabeling. *Nat Protoc* 2: 2480 – 2491

Stocking C, Kozak CA (2008) Murine endogenous retroviruses. *Cell Mol Life Sci* 65: 3383 – 3398

Sugiura K, Stock CC (1952) Studies in a tumor spectrum. I. Comparison of the action of methylbis (2-chloroethyl)amine and 3-bis(2-chloroethyl) aminomethyl-4-methoxymethyl −5-hydroxy-6-methylpyridine on the growth of a variety of mouse and rat tumors. *Cancer* 5: 382 – 402

The M, MacCoss MJ, Noble WS, Kall L (2016) Fast and accurate protein false discovery rates on large-scale proteomics data sets with Percolator 3.0. *J Am Soc Mass Spectrom* 27: 1719 – 1727

Thery C, Regnault A, Garin J, Wolfers J, Zitvogel L, Ricciardi-Castagnoli P, Raposo G, Amigorena S (1999) Molecular characterization of dendritic cell-derived exosomes. Selective accumulation of the heat shock protein hsc73. *J Cell Biol* 147: 599 – 610

Thery C, Boussac M, Veron P, Ricciardi-Castagnoli P, Raposo G, Garin J, Amigorena S (2001) Proteomic analysis of dendritic cell-derived exosomes: a secreted subcellular compartment distinct from apoptotic vesicles. *J Immunol* 166: 7309 – 7318

Thery C, Amigorena S, Raposo G, Clayton A (2006) Isolation and characterization of exosomes from cell culture supernatants and biological fluids. *Curr Protoc Cell Biol* Chapter 3: Unit 3.22

Thery C, Ostrowski M, Segura E (2009) Membrane vesicles as conveyors of immune responses. *Nat Rev Immunol* 9: 581 – 593

Thery C, Witwer KW, Aikawa E, Alcaraz MJ, Anderson JD, Andriantsitohaina R, Antoniou A, Arab T, Archer F, Atkin-Smith GK *et al* (2018) Minimal information for studies of extracellular vesicles 2018 (MISEV2018): a position statement of the International Society for Extracellular Vesicles and update of the MISEV2014 guidelines. *J Extracell Vesicles* 7: 1535750

Tkach M, Kowal J, Zucchetti AE, Enserink L, Jouve M, Lankar D, Saitakis M, Martin-Jaular L, Thery C (2017) Qualitative differences in T-cell activation by dendritic cell-derived extracellular vesicle subtypes. *EMBO J* 36: 3012 – 3028

Tkach M, Kowal J, Thery C (2018) Why the need and how to approach the functional diversity of extracellular vesicles. *Philos Trans R Soc Lond B Biol Sci* 373: 20160479

Valenzuela JI, Perez F (2020) Localized intercellular transfer of ephrin-as by trans-endocytosis enables long-term signaling. *Dev Cell* 52: 104 – 117

Valot B, Langella O, Nano E, Zivy M (2011) MassChroQ: a versatile tool for mass spectrometry quantification. *Proteomics* 11: 3572 – 3577

Veron P, Segura E, Sugano G, Amigorena S, Thery C (2005) Accumulation of MFG-E8/lactadherin on exosomes from immature dendritic cells. *Blood Cells Mol Dis* 35: 81 – 88

Vremec D, Segura E (2013) The purification of large numbers of antigen presenting dendritic cells from mouse spleen. *Methods Mol Biol* 960: 327 – 350

Whiteside TL (2008) The tumor microenvironment and its role in promoting tumor growth. *Oncogene* 27: 5904 – 5912

Williams C, Royo F, Aizpurua-Olaizola O, Pazos R, Boons GJ, Reichardt NC, Falcon-Perez JM (2018) Glycosylation of extracellular vesicles: current knowledge, tools and clinical perspectives. *J Extracell Vesicles* 7: 1442985

Willms E, Cabanas C, Mager I, Wood MJA, Vader P (2018) Extracellular vesicle heterogeneity: subpopulations, isolation techniques, and diverse functions in cancer progression. *Front Immunol* 9: 738

Wolfers J, Lozier A, Raposo G, Regnault A, Thery C, Masurier C, Flament C, Pouzieux S, Faure F, Tursz T *et al* (2001) Tumor-derived exosomes are a source of shared tumor rejection antigens for CTL cross-priming. *Nat Med* 7: 297 – 303

Young GR, Eksmond U, Salcedo R, Alexopoulou L, Stoye JP, Kassiotis G (2012) Resurrection of endogenous retroviruses in antibody-deficient mice. *Nature* 491: 774 – 778

Zeelenberg IS, Ostrowski M, Krumeich S, Bobrie A, Jancic C, Boissonnas A, Delcayre A, Le Pecq JB, Combadiere B, Amigorena S *et al* (2008) Targeting tumor antigens to secreted membrane vesicles *in vivo* induces efficient antitumor immune responses. *Cancer Res* 68: 1228 – 1235

Zhang H, Freitas D, Kim HS, Fabijanic K, Li Z, Chen H, Mark MT, Molina H, Martin AB, Bojmar L *et al* (2018) Identification of distinct nanoparticles and subsets of extracellular vesicles by asymmetric flow field-flow fractionation. *Nat Cell Biol* 20: 332 – 343

Zhang Q, Higginbotham JN, Jeppesen DK, Yang YP, Li W, McKinley ET, Graves-Deal R, Ping J, Britain CM, Dorsett KA *et al* (2019) Transfer of functional cargo in exomeres. *Cell Rep* 27: 940 – 954

Zhang Q, Jeppesen DK, Higginbotham JN, Franklin JL, Crowe JE Jr, Coffey RJ (2021a) Angiotensin-converting enzyme 2-containing small extracellular vesicles and exomeres bind the severe acute respiratory syndrome coronavirus 2 spike protein. *Gastroenterology* 160: 958 – 961

Zhang Q, Jeppesen DK, Higginbotham JN, Graves-Deal R, Trinh VQ, Ramirez MA, Sohn Y, Neininger AC, Taneja N, McKinley ET *et al* (2021b) Supermeres are functional extracellular nanoparticles replete with disease biomarkers and therapeutic targets. *Nat Cell Biol* 23: 1240 – 1254